TECHNISCHE UNIVERSITÄT MÜNCHEN

Lehrstuhl für Hochfrequenztechnik

Theoretical and Experimental Investigation of the Tunable Mobile Antenna.
Model, Designing Procedure and Measurement Methods

Libo Huang

Vollständiger Abdruck der von der Fakultät für Elektrotechnik und Informationstechnik der Technischen Universität München zur Erlangung des akademischen Grades eines

Doktor-Ingenieurs

genehmigten Dissertation.

Vorsitzender: Univ.-Prof. Dr. sc. techn. A. Herkersdorf

Prüfer der Dissertation:

1. Univ.-Prof. Dr. techn. P. Russer
2. Univ.-Prof. Dr.-Ing., Dr.-Ing.habil. St. Lindenmeier, Universität der Bundeswehr München

Die Dissertation wurde am 21.04.2008 bei der Technischen Universität München eingereicht und durch die Fakultät für Elektrotechnik und Informationstechnik am 03.12.2008 angenommen.

Acknowledgement

I would like to express my sincere gratitude and appreciation to my supervisor Professor Peter Russer for his advice, guidance and patience throughout my Ph.D study.

The major support during my study is from Dr. Werner L. Schroeder, who is my tutor in the companies. He provided me with the opportunity of the Ph.D study, accompanied me from Siemens Mobile to BenQ Mobile, from the small but beautiful town Bocholt to the even smaller Kamp-Lintfort. I have really learnt a lot from you, especially the scientific way of thinking. I think all your students have been affected by your personality.

I would like to thank Dr. Uwe Siart who put a lot of time on my Ph.D thesis and gave me so many advices.

I would like to thank Mr. Asim Amin, Mr. Dirk van Almsick and Mr. Shameem Chaudhury who helped me fabricate the demonstrators. Special thank should be given to Mr. Chaudhury, who fabricated the final demonstrator, and helped me with all the measurements in the unforgettable time.

I would like to thank the Ernst von Siemens Foundation for the financial support of this project.

I would like to thank my parents, who sent me abroad, and always worry about me. I wish in the past 3 years, I had not brought you too much trouble.

I would like to thank all my former and current colleagues in the companies and university, who are willing to share the precious practical experience with me. I was deeply moved when you ran through the whole company just to search a short cable.

I would like to thank my friends all around the world. I really want to list all of you. During the tough time of my study, it is the encouragement from you that drives me fighting back again and again. I have recorded all the stories with you in my diary and I will remember you forever.

Munich, November 2007

Libo Huang

Contents

Abstract

Today, more and more mobile services are emerging: GSM 850, GSM 900, PCS 1800, DCS 1900, UMTS, DVB-H, WLAN, etc. The mobile antennas are required to support an increasing number of bands. On the other hand, due to the trend towards miniaturization, the available space inside the mobile phones for the antennas decreases. As the attainable antenna bandwidth is subjected to the physical limit depending on the size of the mobile terminal, it becomes impractical for a mobile antenna to cover all the bands with satisfactory reflection magnitude.

The high-efficiency tunable antenna which covers a large bandwidth with low return loss is a promising solution to this problem. Limitations of the tunable antennas are their loss and non-linearity introduced by the tuning devices.

The physical limit on the attainable bandwidth of the mobile terminal is shown first. This limit is applied to the DVB-H standard, which is a broadband application. The result shows that the non-tunable antenna can not cover the whole DVB-H band with satisfactory reflection magnitude. Solution approaches for the tunable mobile antenna design are proposed in detail, including the designing procedure, device selection, low-loss tuning circuit design and harmonics suppression. New measurement set-ups for tunable antennas are proposed. The demonstrators are shown in the end.

Chapter 1

Introduction

1.1 Background

Today and even more in the future, the number of the mobile services is constantly increasing. A selection of the mobile bands currently in use are listed in Tab. 1.1. Future mobile antennas will be required to cover all those bands with low return loss, high efficiency and sufficiently small nonlinearity.

The attainable antenna bandwidth is limited physically depending on the size of the mobile phone [1][2][3]. Due to the trend towards miniaturization, the size of the mobile phones as well as the space available for the mobile antenna are shrinking. The antenna designer has to consider on the design goals of the mobile phone, its shape, the arrangement of the components and the available space and possible position of the antenna. As a result, it is difficult to build a mobile antenna to cover all the required bands with good impedance match. The most challenging task comes in the lowband applications, e.g. DVB-H, GSM 850 and GSM 900, where the operating wavelength in air considerably exceeds the size of the whole mobile phone.

Tunable antenna is a promising solution to this problem. By introducing tuning devices and circuits into the antenna, the resonance frequency of the antenna can be electrically tuned. Past research on the tunable antenna for mobile phone was taken by different groups, including Auckland and Aberle [4][5][6], Kivekäs and Ollikainen[7], Karmakar[8][9], our group[10] and Suzuki[11].

Critical issues of mobile tunable antennas are size, efficiency and linearity.

1.2 Objectives

The main aim of this thesis is to propose a systematic design procedure for the tunable mobile antenna. As the mobile antenna engineers have limited degrees of freedom to choose the radiating structure of the antenna, this

Name	Operating band (MHz)	Bandwidth (MHz)
DVB-H	470 ··· 862	392
GSM 850	824 ··· 894	70
EGSM 900	880 ··· 960	80
DCS 1800	1710 ··· 1785	75
PCS 1900	1850 ··· 1910	60
UMTS (Europe)	1885 ··· 2025 2110 ··· 2200	40 90
Bluetooth & Wi-Fi & Wireless LAN	2400 ··· 2485	85
WiMax		around 500

Table 1.1: A selection of the mobile communication services and the corresponding frequency bands.

work will mainly focus on the development of tuning mechanisms including selection of the tuning devices, design of the tuning circuits, suppression and compensation of the nonlinear effects, etc. In addition, new measurement set-ups for the tunable antennas are proposed.

1.3 Organization of the thesis

This thesis is organized in the following way. Chapter 2 gives the physical upper limit on the attainable bandwidth of the mobile antenna. The limit shows that it is impractical for a non-tunable antenna to cover all the bands with satisfactory return loss. And the existing solutions for this problem are listed. Chapter 3 proposes the tunable antenna design procedure, including designing non-tunable prototype antenna, estimating number of tuning states, introducing and selecting tuning devices. Chapter 4 proposes the tunable antenna measurement set-ups and procedures. Chapter 5 presents the demonstrators. The conclusion is given in Chapter 6. The Appendix presents the standardized requirements on mobile phones and the basics of TLM method, which is used for the antenna modeling.

Chapter 2

State of the Art

2.1 Physical limitation on the attainable bandwidth

Due to the small size of the mobile phone, the mobile antenna is an electrically small antenna, whose geometrical dimensions are small compared to the wavelengths of the radiated electromagnetic fields. More specifically, the electrically small antenna is any antenna which fits inside a sphere of radius $a = \lambda/2\pi$ where λ is the operating wavelength in air. The radiation properties of the electrically small antennas were first investigated by Wheeler [12]. Later, a very comprehensive theory was published by Chu [1] in which the minimum radiation quality factor Q of a linear polarized antenna, which fits inside a sphere of an given radius, was derived. Harrington extended this theory to include circular polarized antennas [13]. Collin [14] and later Fante [15] published an exact theory based on calculating the evanescent energy stored around the antenna. The most recent result was published by McLean [2] as a re-examination of the fundamental limit.

The quality factor Q of an electrical network at resonance is defined as

$$Q = \frac{\omega W_{\text{store}}}{P}, \tag{2.1}$$

where ω is the operating frequency, W_{store} is the time-average energy stored in the network and P is the power dissipated in the networks. When the network is not at resonance, the input impedance is proportional to $P + 2\text{j}\omega(W_{\text{m}} - W_{\text{e}})$, where W_{m} and W_{e} are the time-average magnetic and electric energy stored in the network. To make the input impedance resistive, some additional energy storage must be added so that the net reactive energy vanishes. If it is assumed that the network is operated with an additional ideal lossless reactive element so that the input impedance is real, the Q of the resultant network is

$$Q = \frac{2\omega W}{P}, \tag{2.2}$$

with W the larger of W_{m} and W_{e}.

Considering an antenna enclosed in a sphere of radius a, the field for $r > a$ may be expressed in terms of an expansion in orthogonal TE_{nm} and TM_{nm} modes, where n is the order of the spherical Bessel functions, and m is the azimuthal variation [14]. Since these modes are orthogonal, the radiated power and stored reactive energy is the sum of those contributed by each mode. The Q of a TE_{nm} mode is independent of the azimuthal mode index m, and hence it is sufficient to evaluate it for $m = 0$ only [14]. The TM_{nm} mode is the dual of the TE_{nm} mode, it has the same Q but with the stored electric energy greater than the stored magnetic energy [14].

The field components for a TM_{n0} mode are [14]

$$E_\theta = \frac{-k_0 \sin\theta}{\mathrm{j}\omega\epsilon_0 r} P_n'(\cos\theta)[k_0 r h_n(k_0 r)]', \tag{2.3}$$

$$E_r = \frac{1}{\mathrm{j}\omega\epsilon_0} \frac{n(n+1)}{r^2} P_n(\cos\theta)[k_0 r h_n(k_0 r)], \tag{2.4}$$

$$H_\phi = \frac{\sin\theta}{r} P_n'(\cos\theta)[k_0 r h_n(k_0 r)], \tag{2.5}$$

where the prime denotes differentiation with respect to the argument, P_n is the Legendre polynomial, and h_n is the spherical Hankel function of the second kind.

Integration of the complex Poynting vector over the sphere $r = a$ yields [14]

$$\begin{aligned} &\frac{1}{2}\int_0^{2\pi}\int_0^{\pi} E_\theta H_\phi^* a^2 \sin\theta \,\mathrm{d}\phi \,\mathrm{d}\theta \\ &\qquad = P_\mathrm{r} + 2\mathrm{j}\omega(W_\mathrm{m} - W_\mathrm{e}) \\ &\qquad = \frac{k_0\pi}{\omega\epsilon_0}\frac{2n(n+1)}{2n+1} + \mathrm{j}\frac{k_0}{\omega\epsilon_0}\frac{2n(n+1)}{2n+1} \\ &\qquad \cdot \{j_n(k_0 r)[k_0 r j_n(k_0 r)]' - y_n(k_0 r)[k_0 r y_n(k_0 r)]'\}|_{r=a}, \end{aligned} \tag{2.6}$$

where P_r is the total radiated power, $W_\mathrm{m} - W_\mathrm{e}$ is the net reactive energy stored in the field, j_n and y_n are the spherical Bessel functions of the first and second kinds. After integration over θ and ϕ, the total time-average stored energy in the field is [14]

$$\begin{aligned} W_\mathrm{m} + W_\mathrm{e} = &\frac{\mu_0\pi}{2}\frac{2n(n+1)}{2n+1}\int_a^\infty \left\{ \left[1 + \frac{n(n+1)}{k_0^2 r^2}\right] \right. \\ &\cdot (k_0 r)^2 h_n(k_0 r) h_n^*(k_0 r) \\ &\left. + [k_0 r h_n(k_0 r)]'[k_0 r h_n^*(k_0 r)]' \right\} \mathrm{d}r. \end{aligned} \tag{2.7}$$

Since this expression includes the energy in the evanescent field and also that in the radiated field, to obtain the energy stored in the evanescent field,

the energy density associated with the radiation field must be subtracted [14]. The energy associated with the radiation field is the real part of the radial component of the complex Poynting vector divided by the velocity of energy flow [14]. After integration over θ and ϕ from Eq. 2.6, this is [14]

$$(\mu_0\epsilon_0)^{1/2}P_{\mathrm{r}} = \frac{k_0\pi}{\omega\epsilon_0}(\mu_0\epsilon_0)^{1/2}\frac{2n(n+1)}{2n+1}. \tag{2.8}$$

Thus, the energy stored in the evanescent field is [14]

$$\begin{aligned}(W_{\mathrm{m}}+W_{\mathrm{e}})_{\mathrm{e}} =& \frac{n(n+1)}{2n+1}\frac{\mu_0\pi}{k_0} \\ & \cdot\{2k_0a-(k_0a)^3[j_n^2+y_n^2-j_{n-1}j_{n+1} \\ & -y_{n-1}y_{n+1}]-(k_0a)^2[j_nj_n'+y_ny_n'] \\ & -k_0a[j_n^2+y_n^2]\},\end{aligned} \tag{2.9}$$

where the Bessel functions are all evaluated at $\rho = k_0a$.

The quality factor of the TM_{n0} mode, denoted by Q_n is [14]

$$\begin{aligned}Q_n =& \frac{2\omega(W_{\mathrm{e}})_{\mathrm{e}}}{P_{\mathrm{r}}} \\ =& k_0a-\left(\frac{k_0a}{2}+\frac{n+1}{k_0a}\right)(C_n^2+D_n^2) \\ & +\left(n+\frac{3}{2}\right)(C_nD_{n+1}-D_nC_{n+1}) \\ & -\frac{(k_0a)^2}{2}(C_{n+1}^2+D_{n+1}^2),\end{aligned} \tag{2.10}$$

where

$$\begin{aligned}C_n &= \sum_{m=0}^{2m\le n}\frac{(-1)^m(n+2m)!}{(2m)!(n-2m)!2^{2m}(k_0a)^{2m}}, \\ D_n &= \sum_{m=0}^{2m\le n-1}\frac{(-1)^m(n+2m+1)!}{(2m+1)!(n-2m-1)!2^{2m+1}(k_0a)^{2m+1}}.\end{aligned} \tag{2.11}$$

TM_{10} mode has the lowest quality factor [1][14], which is

$$Q_1 = \frac{1}{k_0a}+\frac{1}{(k_0a)^3}. \tag{2.12}$$

This is the minimum radiation quality factor of the linear antenna which can be enclosed in a sphere with radius a [2].

The upper limit on the attainable fractional impedance bandwidth ($b = \frac{f_{\max}-f_{\min}}{\sqrt{f_{\max}f_{\min}}}$) of the antenna can be found from Q_1 and maximum allowed reflection factor S by [16]

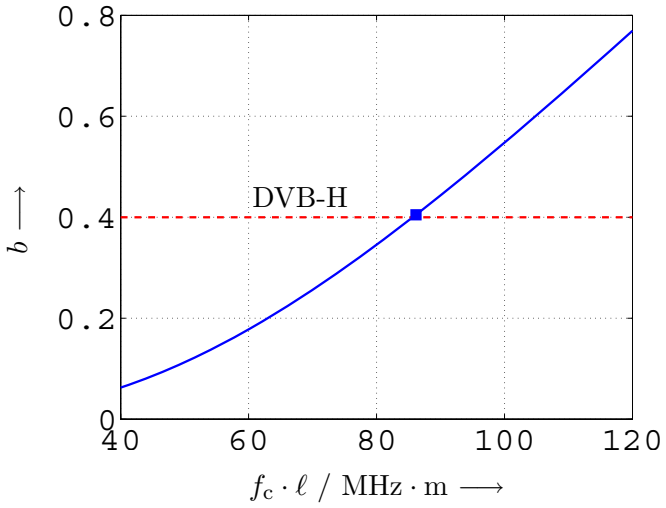

Figure 2.1: The upper limit on 7 dB fractional impedance bandwidth depending on the electrical length of the electrically small antenna. The dashed line denotes the fractional bandwidth of DVB-H (470 - 702 MHz).

$$b = \frac{1}{Q_1}\frac{S-1}{\sqrt{S}}. \tag{2.13}$$

For 7 dB bandwidth, which is normal for mobile antenna, Eq. 2.13 can be written as

$$b = \frac{1}{Q_1}. \tag{2.14}$$

The upper limit on the 7 dB fractional impedance bandwidth depending on the electrical length (product of the physical length and the center frequency) of the electrically small antenna is shown in Fig. 2.1. The dashed line denotes the fractional bandwidth of DVB-H (470 - 702 MHz [17]). Considering the centre frequency of 570 MHz, the antenna should be over 150 mm long in dimension to cover the DVB-H band with maximum -7 dB reflection factor.

Due to the neglection of the energy stored inside the sphere enclosing the antenna, the radiation quality factor is underestimated. The mobile antenna bandwidths achieved in practice are much smaller than what is shown in Fig. 2.1, especially when the operating wavelength in air is much longer than the length of the mobile terminal (lowband).

2.2 Existing solutions

Due to the limited size of the mobile terminal, restricted size and shape of the mobile antenna, the obtained antenna bandwidth is small. The existing

solutions are stated in the following.

Wideband coverage can be achieved also by a small antenna if it is mounted on a large printed circuit board. An inductive coupler for the folded type mobile phone which shows over 10 dB return loss in the 470 to 702 MHz range is reported [18]. The whole size of the printed circuit board was 150 mm ×45 mm.

Antenna bandwidth can be made larger by a matching circuit [16]. A DVB-H antenna mounted on a 130 mm ×75 mm printed circuit board was matched to the 50 Ω port by a matching circuit [19]. The measured maximum return loss in DVB-H band was −1.5 dB.

Electrically tunable antennas mounted on small printed circuit boards can cover wide band with good impedance match. To the knowledge of the author, the first tunable antenna for the mobile phones in public literature was a tunable planar inverted F antenna (PIFA) which is tunable between GSM 850 (824 to 896 MHz) and GSM 900 (890 to 960 MHz) [4] [5] [6] with PIN diodes as the tuning devices. It was fabricated on a 100 mm ×40 mm printed circuit board. This antenna exhibits a relatively large size of 25 mm ×19 mm ×6 mm.

An antenna which was tunable between GSM 850 to GSM 900 with over 7 dB return loss is reported [7]. The antenna was fabricated on a 110 mm ×40 mm printed circuit board and has the size of 16 mm ×38 mm ×8 mm. The tuning device is a single-pole-double-throw switch.

A tunable stacked patch PIFA with RF PIN switch array was designed [8] [9]. It was constructed on a 100 mm ×50 mm printed circuit board and has a large volume of 56 mm ×30 mm ×11 mm. This antenna is tunable in the range from 640 to 1900 MHz, with the maximum return loss of 8 dB.

The DVB-H application imposes a high requirement on the mobile antenna design, due to the low operating frequency and the big fractional bandwidth. Three tunable antennas built up on a long printed circuit board for the folded type mobile phone were constructed with a single-pole-multi-throw RF switch [11]. They were tunable in the range from 470 to 770 MHz. The maximum return loss in the whole frequency range was −4.5 dB.

An antenna tuned by electrical devices like varactor diodes is in principle non-linear. The high-power signal from the GSM transmitter in the mobile phone will be distorted non-linearly due to the tuning devices and harmonics will be generated. The linearity of the tunable antenna is a key requirement in design.

Chapter 3

Tunable Antenna Design

3.1 Non-tunable prototype antenna design

The multi-layer printed circuit board of a mobile phone consists of ground planes with the same size of the printed circuit board. The top and bottom layers of the printed circuit board consist of continuous metal sheets for electromagnetic compatibility shielding. Metal plates are put on the printed circuit board as shown in Fig. 3.1 to provide further shielding. The combination of the ground planes, metal sheets for shielding and the metal plates can be modeled as a solid metal antenna chassis [20]. The effect of the antenna chassis on the whole radiating structure including the antenna chassis and the antenna has been studied for years [21]. The dominant characteristic modes of the surface current on the chassis have major contribution on the radiation of the whole radiating structure. In [22], [21], it was reported that at 900 MHz in a typical mobile phone with 10% fractional bandwidth, the small antenna radiates around 10% of the total radiated power, with most of the power radiated by the half-wave dipole-type current distribution on the chassis, (see e.g. Fig. 3.2) [20]. The numerical analysis of the characteristic modes of the mobile antenna chassis is given in [23]. The characteristic modes of the chassis can be tuned by changing the chassis geometry [24]. In this work, a 110 mm $\times$55 mm rectangular printed circuit board is used as the chassis.

The antenna induces surface currents in the chassis. The most commonly used PIFA in the mobile phones, which is a self-resonant antenna, can not induce the surface current efficiently [20]. A non-resonant antenna element can achieve an efficient chassis mode coupling with a very small volume [22], [26], [18]. An efficient coupling to the chassis mode can be achieved by locating the electric field maximum of the antenna near the electric field maximum of the chassis [20]. An analysis of the interaction between the exciting field generated by the antenna and the characteristic surface current modes on the chassis is done in [23] which states that a very small vertical

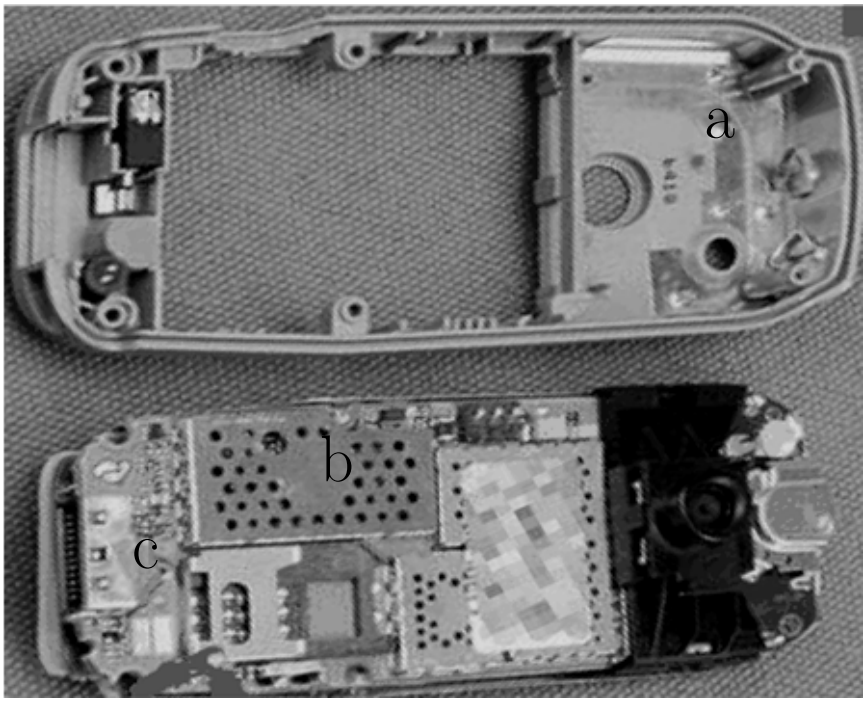

Figure 3.1: Photo of the internal part of one mobile phone, with a) antenna, b) a metal plate for electromagnetic shielding, c) printed circuit board.

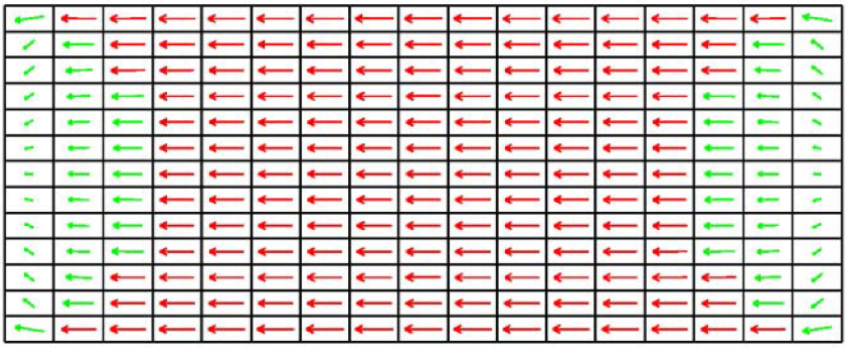

Figure 3.2: Surface current distribution for a half-wave dipole type characteristic mode which resonates at 1.33 GHz for a 100 mm ×40 mm rectangular printed circuit board by [25].

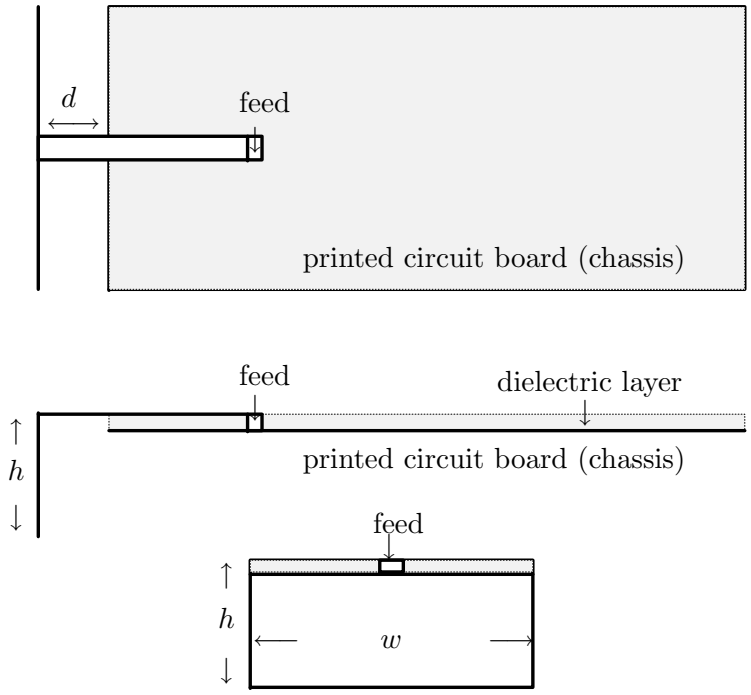

Figure 3.3: Structure of the capacitive coupler, w and h the width and height of the vertical board respectively , and d the distance between the vertical board and the printed circuit board.

board put in front of the short edge of the chassis (shown in Fig. 3.3) will achieve the most efficient coupling with the smallest volume consumption. This structure is called the capacitive coupler. The larger the size of the vertical board $w \times h$ and the longer the distance between the vertical board and the edge of the chassis d, the higher the coupling efficiency.

3.2 TLM model of the capacitive coupler

Fig. 3.4 gives the dimensions of the modeled capacitive coupler. The chassis is chosen as a 110 mm ×56 mm printed circuit board, with the dielectric material of FR4 with $\epsilon_r = 4.6$ in the operating band of interest. FR4 is a common material in the mobile phone applications. The thickness of the dielectric layer is 0.4 mm. The size of the vertical board is 56 mm wide and 10 mm high. The distance between the printed circuit board and the vertical board is 8 mm.

The modeling is done by MEFiSTo-3D Pro provided by Faustus Scientific Corporation, which is based on the Transmission Line Matrix method (TLM). The 50 Ω port is realized by a section of 25 mm long 50 Ω microstrip

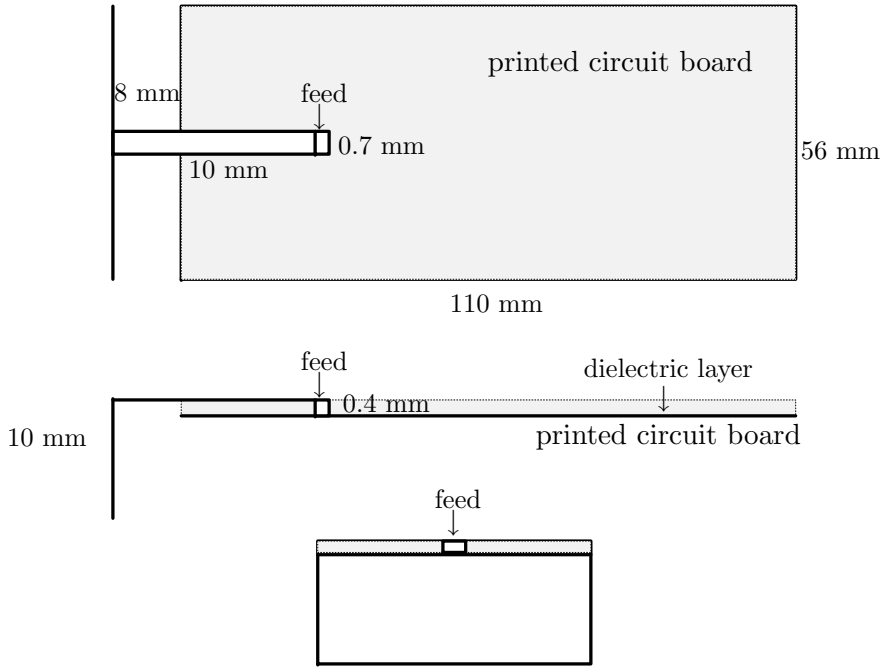

Figure 3.4: The dimensions definition of the modeled capacitive coupler.

line on the printed circuit board. One end of the line section is connected to a source, and the other end is connected to the coupler. A probe is put in the middle of the microstrip line. To extract the scattering parameters, a reference microstrip line section is constructed, with one end connected to a reference source and the other terminated by a perfect absorber. A reference probe is put at the same distance from the reference source as that between the probe and the source in the original structure. Both the antenna structure and the reference microstrip line section are excited with the same pulse. The incident wave is taken as the voltage measured by the probe in the reference microstrip line section, and the reflected wave is taken as the difference between the voltages measured by the two probes. To subtract the phase shift due to the microstrip line between the probe and the end of the coupler part, the deembedding is done by Matlab.

The input impedance of the capacitive coupler simulated by MEFiSTO is plotted in the Smith chart and shown in Fig. 3.5. The reference impedance of the Smith chart is 50 Ω. The real and imaginary part of the input impedance are plotted in Fig. 3.6 and Fig. 3.7 respectively. As a comparison, the same structure is modeled by CST Microwave Studio which is based on Finite-Difference Time-Domain method (FDTD), the result is plotted in Fig. 3.5, Fig. 3.6 and Fig. 3.7 too. The results from the TLM method and the FDTD method are close to each other.

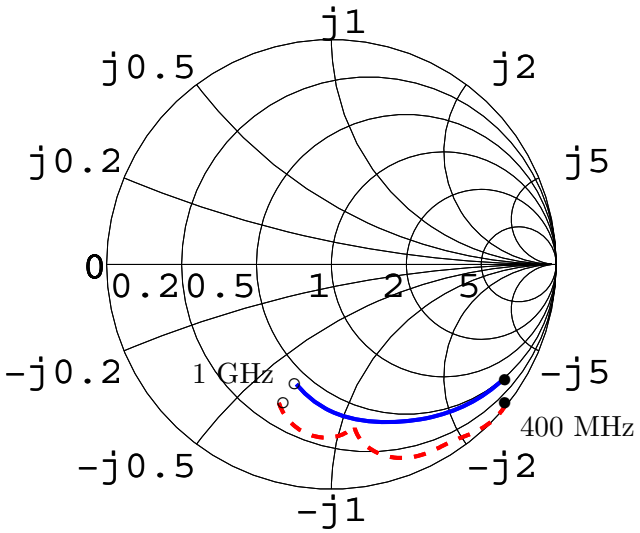

Figure 3.5: Comparison of the input impedance from 400 MHz to 1 GHz of the DVB-H capacitive coupler simulated by MEFiSTO (solid line) and CST Microwave Studio (dashed line). The reference impedance is 50 Ω.

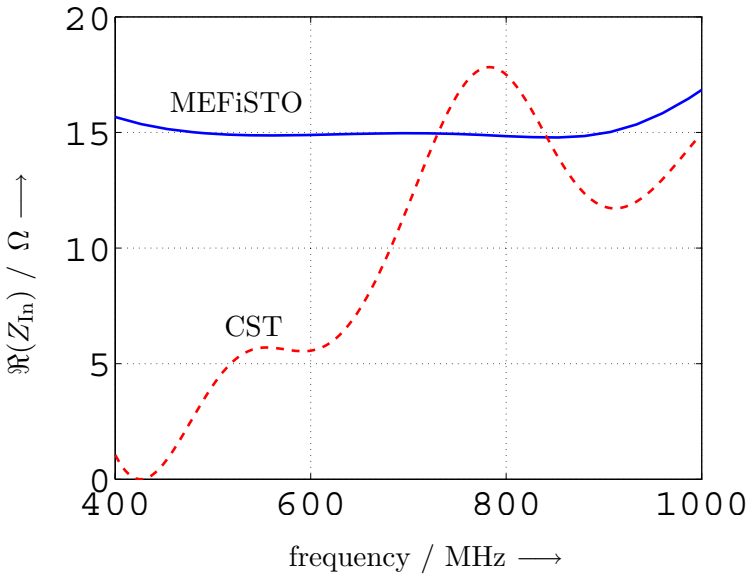

Figure 3.6: Comparison of the real part of the input impedance from 400 MHz to 1 GHz of the DVB-H capacitive coupler simulated by MEFiSTO (solid line) and CST Microwave Studio (dashed line).

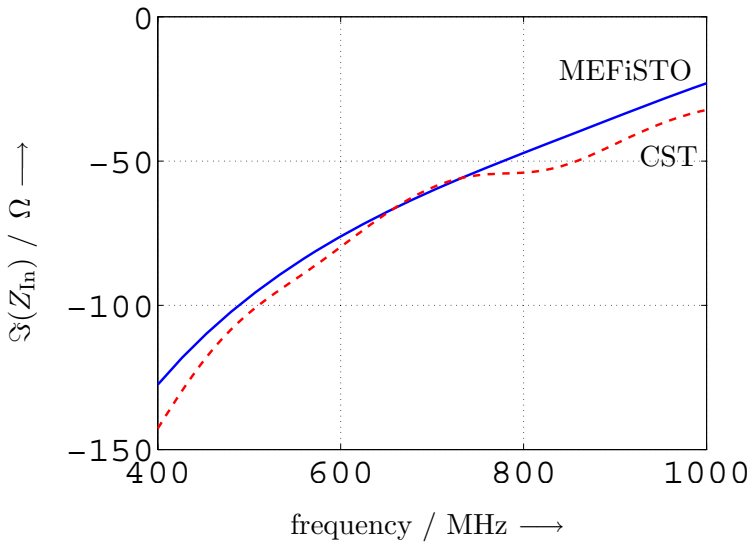

Figure 3.7: Comparison of the imaginary part of the input impedance from 400 MHz to 1 GHz of the DVB-H capacitive coupler simulated by MEFiSTO (solid line) and CST Microwave Studio (dashed line).

3.3 Matching circuit design

3.3.1 Theoretical limit

Fig. 3.5 shows that below 1 GHz the coupler is capacitive. At 570 MHz, the center frequency of the DVB-H band, the simulated input impedance of the capacitive coupler is $5.66 - \mathrm{j}86.9\,\Omega$, which corresponds to the equivalent unloaded quality factor Q of 15.4 calculated as the ratio of the reactance to the resistance. A matching circuit can be used to match this coupler to the 50 Ω port.

The theoretical upper limit of the maximum attainable fractional bandwidth B_n with n matching stages for narrow band application given the quality factor Q of the load and the maximum permissible reflection magnitude R is given by Fano [27] and later reviewed by Lopez [28]. The theoretical upper limit of the product of Q and B_n is

$$QB_n = \frac{1}{b_n \sinh\left[\frac{1}{a_n}\ln\left(\frac{1}{R}\right)\right] + \frac{1-b_n}{a_n}\ln\left(\frac{1}{R}\right)} \text{[28]} \tag{3.1}$$

with the parameters a_n and b_n listed in Tab. 3.1. Tab. 3.2 gives the upper limit on the attainable 7 dB bandwidth with the center frequency of 570 MHz.

n	a_n	b_n
1	1	1
2	2	1
3	2.413	0.678
4	2.628	0.474
5	2.755	0.347
6	2.838	0.264
7	2.896	0.209
8	2.937	0.160
∞	π	0

Table 3.1: The parameters a_n b_n used in Equ. 3.1 to calculate the theoretical upper limit on the fractional attainable bandwidth, by [28].

n	1	2	3	4	5	6	∞
B_n	0.07	0.16	0.19	0.21	0.22	0.23	0.25
Attainable 7 dB bandwidth / MHz	41	89	109	119	126	130	144

Table 3.2: The theoretical upper limit on the attainable bandwidth for the capacitive coupler shown in Fig. 3.4, with nth order matching. B_n denotes the upper limit on the attainable fractional bandwidth.

3.3.2 Matching circuit implementing technologies

There are basically three technologies to implement the matching circuits:

- microstrip lines,
- lumped elements,
- integrated circuits: SAW, LTCC, etc.

The dielectric material used in the printed circuit board for mobile phones is FR4. In DVB-H band, it exhibits the permittivity ϵ_r of 4.5, the loss tangent around 0.015. The operating wavelength of the microstrip line fabricated on FR4 is over 240 mm. In a 100 mm $\times$40 mm mobile phone for instance, the area available for the matching circuit is smaller than 40 mm $\times$20 mm. The microstrip line matching circuit is not feasible.

Integrated matching circuits exhibit the smallest size and low loss. However, the integration technology of the tuning devices with SAW or LTCC circuits is not yet mature. The matching circuit for the capacitive coupler is constructed by the high-Q lumped elements.

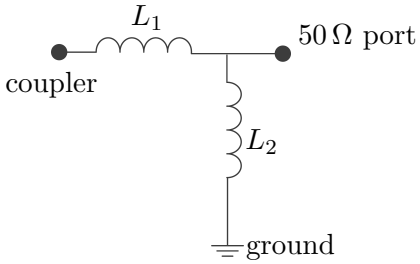

Figure 3.8: Schematic of the matching circuit for the non-tunable prototype DVB-H antenna.

3.3.3 Matching circuit topologies

The upper limit on the attainable bandwidth listed in Tab. 3.2 can be approached by a Chebychev matching network, which is presented in [27], [29]. The drawback of the Chebychev matching network, however, is the requirement of the transformers, which yield losses.

To minimize the losses of the lumped elements especially the inductors, the matching circuit should comprise as few component as possible. As the input impedance of the capacitive coupler shown in Fig. 3.7 is capacitive, a series inductor L_1 is needed to compensate the capacitance. As the real part of input impedance of the coupler is smaller than 50 Ω, either a capacitor C_2 or an inductor L_2 connected in parallel to the 50 Ω feed can be used. A smaller value of L_1 is required when L_2 is used, which leads to lower parasitic resistance and lower loss caused by L_1. Fig. 3.8 shows the schematic of the matching circuit

As the matching circuit is constructed on the printed circuit board and away from the board edges, a full-wave analysis on the matching circuit is not necessary. The matching circuit can be modeled on the basis of a lumped element model. The simulation is done with ADS. The optimal values of L_1 and L_2 are listed in Tab. 3.3 together with the lower and upper boundary frequencies f_{Lower}, f_{Upper} of the maximum attainable 7 dB bands. The optimal value of L_1 decreases from 32 nH to 11 nH while L_2 remains almost unchanged. At least 9 tuning stages are needed to cover the DVB-H bands. The attainable instantaneous bandwidth increases with the increase of the center frequency, because the coupling between the capacitive coupler and the printed circuit board becomes more efficient when the operating frequency approaches the resonance frequency of the printed circuit board which is around 1 GHz [21].

L_1 / nH	L_2 / nH	f_{Lower} / MHz	f_{Upper} / MHz
32	5	470	483
30	5	482	496
28	5	493	511
26	5	505	528
23	5	527	554
20	5	553	583
17	5.5	578	612
14	5.5	609	650
11	6.5	635	710

Table 3.3: The optimal values of L_1 and L_2 of the matching circuit (shown in Fig. 3.8) to match the capacitive coupler to the 50 Ω port in DVB-H band. f_{Lower} and f_{Upper} are the lower and upper boundary frequencies of the attainable 7 dB band.

3.4 Tunable antenna modeling

The modeling of the tunable antenna requires the modeling of the capacitive coupler and the tunable matching circuit. As many devices are introduced into the antenna, especially those that can not be characterized as L, R, C's, e.g. semiconductor switches, commercial antenna simulation softwares are insufficient.

On the other hand, for the capacitive coupler, as the tunable matching circuit is constructed on the printed circuit board, e.g. Fig. 3.10, due to the thin dielectric layer of the printed circuit board, the electromagnetic field of tunable matching circuit is concentrated within the printed circuit board and the radiation effect of this part is negligible.

The mobile antenna can thus be divided into two parts, the radiator, which consists of the coupler and the printed circuit board, and the tunable matching circuit which is constructed on printed circuit board and where electrical devices are placed. The radiator can be modeled by the TLM (Transmission Line Matrix) method, the FDTD (Finite Difference Time Domain) method, etc. And the tunable matching circuit can be modeled on the basis of a lumped element model.

At first, the structure of the radiator is simulated by CST Microwave Studio which is based on FDTD. The reflection coefficients at the port is exported to SnP files, imported to Agilent Design System (ADS) and connected to the tunable matching circuit.

3.4.1 The modeled reflection magnitude at the port

Fig. 3.9 shows the comparison between the reflection magnitude over frequency from the modeling (solid lines) and the measurement (dashed line) of the tunable DVB-H antenna with EGSM coupler on the same printed circuit board, which is shown in Fig. 3.14, for tuning voltage in the range from 0.5 to 4 V. Good agreement between the results from the modeling and the measurement is shown.

3.4.2 Modeling of the antenna efficiency

The loss of the tunable antenna can be classified into two parts, one is the conductive and dielectric loss in the radiator, due to the finite conductivity of the metal and the finite loss tangent of the dielectric material. The software IE3D based on the Method of Moment provided by Zealand can calculate the radiation efficiency η_{radiator} of this part.

The other part is the loss of the tunable matching circuit part caused by the lossy electrical devices and the transmission lines. As shown in Fig. 3.11, the input impedance of the radiator which is the load of this matching circuit is not 50 Ω, the efficiency of the circuit part does not equal to its insertion loss measured by attaching two 50 Ω ports at both ends. The efficiency of the circuit part η_{circuit} is defined by

$$\eta_{\text{circuit}} = \frac{\text{Re}\{V_{\text{out}} \cdot I_{\text{out}}^*\}}{\text{Re}\{V_{\text{in}} \cdot I_{\text{in}}^*\}}. \tag{3.2}$$

For different tuning states, the calculated η_{circuit} at each center frequencies f_c together with the corresponding η_{radiator} simulated by IE3D are listed in Table 3.4. The radiation efficiency η_{rad} of the antenna should be

$$\eta_{\text{rad}} = \eta_{\text{circuit}} \cdot \eta_{\text{radiator}}. \tag{3.3}$$

The antenna efficiency η_{ant} of the antenna takes the loss of power due to the mismatch at the input into account, which can be written as

$$\eta_{\text{ant}} = \eta_{\text{rad}} \cdot (1 - |\Gamma|^2), \tag{3.4}$$

with Γ the reflection factor at the antenna port.

A tunable antenna with the tuning circuit shown in Fig. 3.12 is constructed (shown in Fig. 3.10). The radiation efficiency of this antenna is measured by the method of Wheeler cap following [30]. The antenna efficiency is calculated by Eq. 3.4 with the measured radiation efficiency and the measured reflection factor at the antenna port. Fig. 3.13 compares the η_{ant} from the modeling and the measurement. They agree with each other quite good, especially in the upper half of the band when the control-FET is “on”.

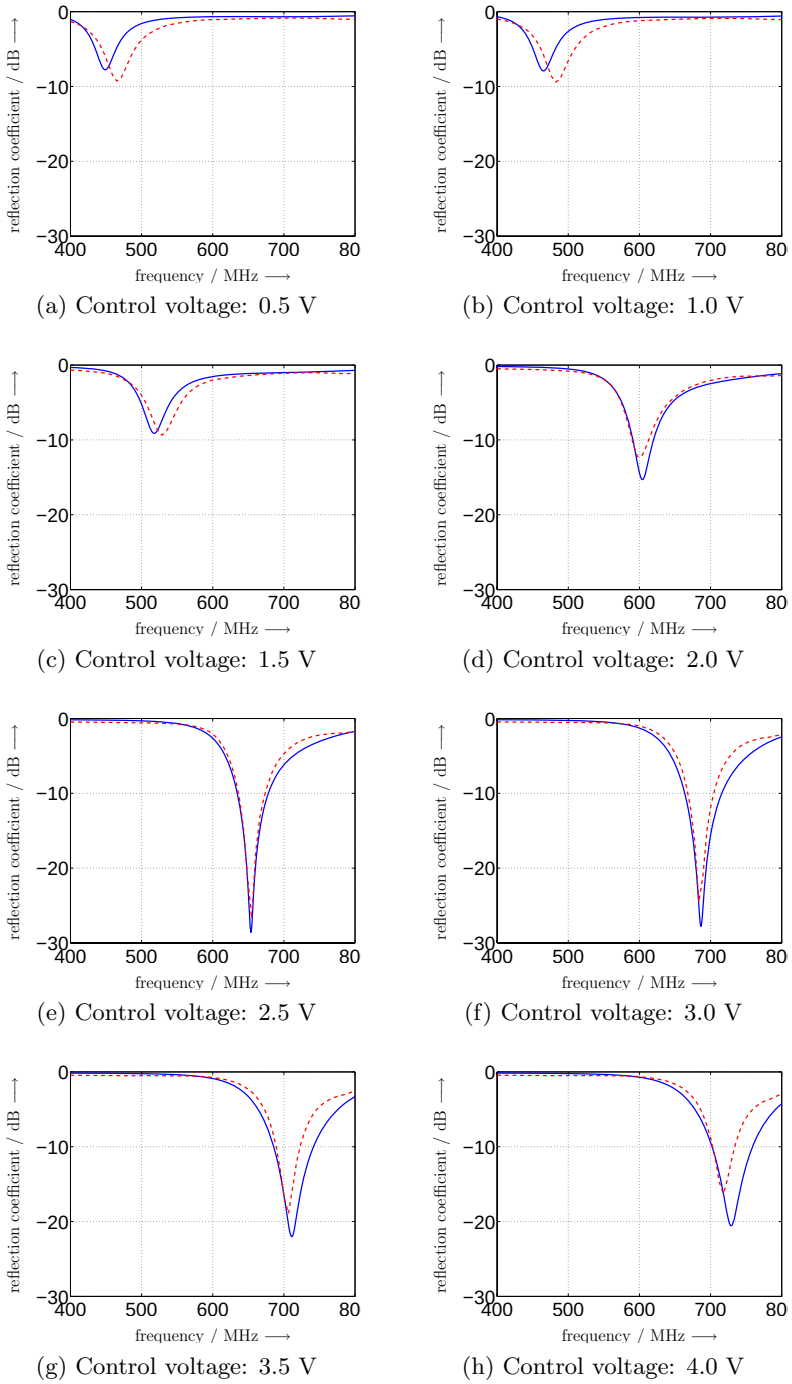

(a) Control voltage: 0.5 V (b) Control voltage: 1.0 V

(c) Control voltage: 1.5 V (d) Control voltage: 2.0 V

(e) Control voltage: 2.5 V (f) Control voltage: 3.0 V

(g) Control voltage: 3.5 V (h) Control voltage: 4.0 V

Figure 3.9: Comparison of the reflection coefficient over frequency from the modeling (solid lines) and the measurement (dashed line) of the tunable DVB-H antenna with EGSM coupler on the same printed circuit board for tuning voltage in the range from 0.5 to 4 V.

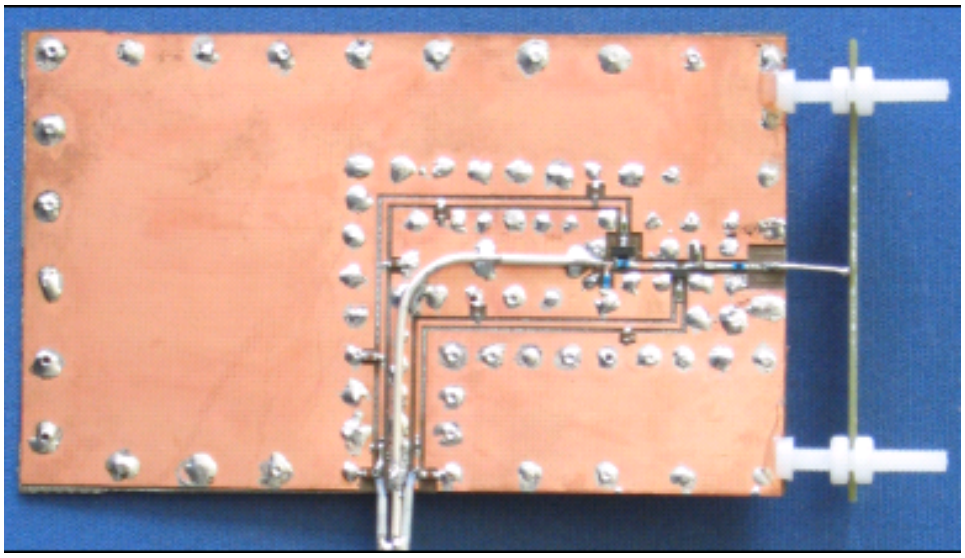

Figure 3.10: Photo of a low-profile DVB-H tunable antenna (version 1), with its tuning circuit constructed by an ASVP (anti-series varactor pair) and a control-FET shown in Fig. 3.12.

f_c / MHz	455.5	461	489.5	513.5	539.5	587.5
η_{circuit} / %	23.5	24.1	26.3	27.8	28.7	28.7
η_{radiator} / %	77.7	78.5	82.2	84.8	87.2	90.8
η_{rad} / %	18.3	18.9	21.6	23.6	25.0	26.1
$\lvert\Gamma\rvert$ / dB	−17	−17	−14	−13	−12	−13
η_{ant} / %	17.9	18.5	20.8	22.4	23.5	24.8
f_c / MHz	591.5	610	623	640	675.5	714
η_{circuit} / %	56.7	57.3	60.0	61.2	64.6	67.7
η_{radiator} / %	91.0	92.1	92.7	93.5	94.9	96.0
η_{rad} / %	51.6	52.8	55.6	57.2	61.3	65.0
$\lvert\Gamma\rvert$ / dB	−13	−13	−14	−14	−17	−21
η_{ant} / %	49.0	50.1	53.4	54.9	60.1	64.5

Table 3.4: The calculated values of the efficiency of the circuit part η_{circuit}, the simulated values of the radiation efficiency of the coupler part η_{radiator} by IE3D, the calculated radiation efficiency η_{rad} based on Eq. 3.3, the modelled magnitude of reflection factor $|\Gamma|$ in dB at the antenna port and the modeled antenna efficiency η_{ant} based on Eq. 3.4, when the instantaneous band is tuned to different center frequencies f_c. The modelled antenna is the DVB-H tunable antenna constructed by an anti-series varactor pair (ASVP) and a control-FET, shown in Fig. 3.10.

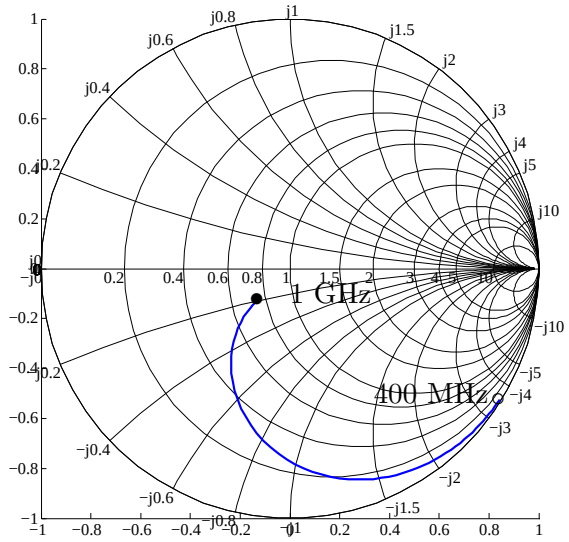

Figure 3.11: Simulated input impedance of the coupler part of a DVB-H tunable antenna (shown in Fig. 3.10) constructed by an anti-series varactor pair (ASVP) and a control-FET from 400 MHz up to 1 GHz.

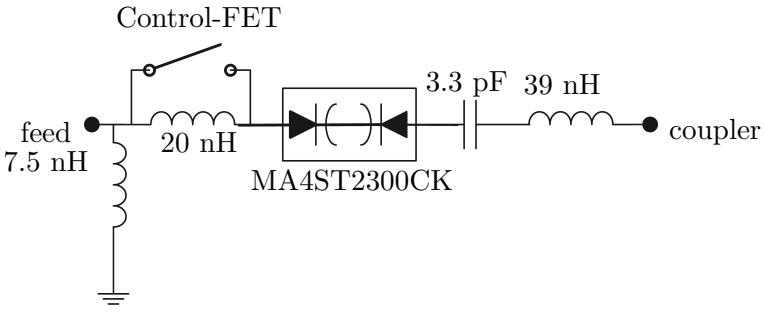

Figure 3.12: Schematic of the tunable matching circuit for a DVB-H tunable antenna (shown in Fig. 3.10) constructed by an anti-series varactor pair (ASVP) and a control-FET.

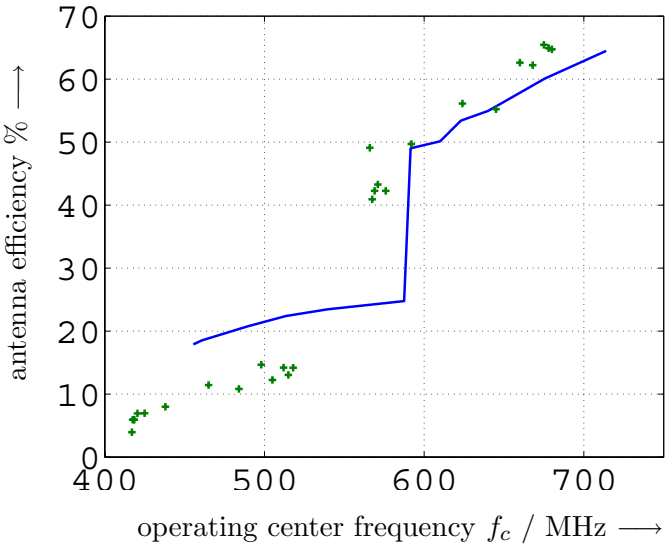

Figure 3.13: The measured antenna efficiency η_{ant} of the DVB-H tunable antenna constructed by an anti-series varactor pair (ASVP) and a control-FET, shown in Fig. 3.10 at different operating center frequency f_c by the Wheeler cap measurement (plottd in dots) and the estimated antenna efficiency (plotted in line) by Tab. 3.4, Eq. 3.3, Eq. 3.4.

3.4.3 Modeling of the harmonics radiation

The most critical non-linearity issue for the tunable antennas is the harmonics radiation. For all the applications with GSM, the harmonics radiation should not exceed $-30\,\mathrm{dBm}$, in the presence of $33\,\mathrm{dBm}$ uplink power [31].

The non-linearity of the tunable antennas can be modeled in either the time domain or the frequency domain. The time domain simulation method requires long simulated time to reach the steady state. The simulated time can be estimated by the following way. Considering that in modeling, the tunable antenna is excited by a sinusoidal wave at frequency f_0 with the average power of P_0, and the simulated time in the time-domain simulator is ΔT. The excited signal can be viewed as a product of an ideal sinusoidal signal and a rectangle signal with the width of ΔT. The spectrum of the excited signal is

$$S(f) = \sqrt{P_0}\frac{\Delta T}{\sqrt{2\pi}}\mathrm{sinc}\left((f-f_0)\Delta T\right)e^{-\mathrm{j}2\pi\frac{\Delta T}{2}(f-f_0)}. \tag{3.5}$$

In simulation, to detect the harmonics generated by the non-linear circuit with the power of P_{har} at $n\cdot f_0$, the ratio $\frac{|S(n\cdot f_0)|^2}{|S(f_0)|^2}$ of the exciting signal should be smaller than the ratio $\frac{P_{\mathrm{har}}}{P_0}$, i.e.

$$\frac{|S(n\cdot f_0)|^2}{|S(f_0)|^2} = \mathrm{sinc}^2((n-1)f_0\Delta T) \le \frac{1}{((n-1)f_0\Delta T)^2} \le \frac{P_{\mathrm{har}}}{P_0} \tag{3.6}$$

with $n = 2, 3, 4\cdots$. As for the second harmonics frequency $2f_0$, $\frac{1}{((n-1)f_0\Delta T)^2}$ has the largest value, thus

$$\Delta T \ge \frac{\sqrt{P_0/P_{\mathrm{har}}}}{f_0}. \tag{3.7}$$

For example, if $P_0 = 33\,\mathrm{dBm}$, $P_{\mathrm{har}} = -30\,\mathrm{dBm}$, $f_0 = 900\mathrm{MHz}$, ΔT should be over $1.57\ \mu\mathrm{s}$. On the other hand, due to the fine meshing required for the mobile antenna, Δt, the resolution in time is smaller than 1 ps, which leads to an unfeasibly large number of time steps. So the frequency domain harmonic balance method is used to model the harmonics radiation.

The radiator is modeled with finite-difference time-domain method (FDTD) by CST Microwave Studio, and the circuit part is modeled by harmonic balance by ADS. The harmonics voltages U_{har} at the input ports of the coupler part can be found by the harmonic balance. The harmonics currents I_{har} at the input ports of the coupler part can be calculated by

$$I_{\mathrm{har}} = \mathbf{Y}U_{\mathrm{har}}, \tag{3.8}$$

with $\mathbf{Y}$ the admittance matrix of the coupler part.

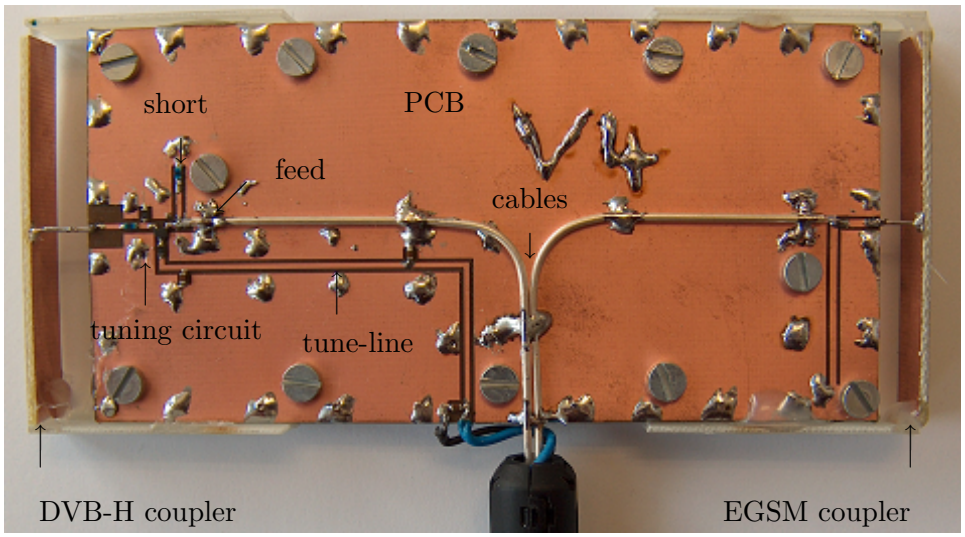

Figure 3.14: Photo of the tunable DVB-H antenna to test the model of harmonics radiation, together with an EGSM antenna attached to a 110 mm $\times$55 mm PCB. Its tunable matching circuit is shown in Fig. 3.15.

The harmonics power P_{har} entering into the coupler part is

$$P_{\text{har}} = \frac{1}{2} U_{\text{har}} I_{\text{har}}^{\dagger}, \tag{3.9}$$

with †, the complex transverse operator on the vector.

In practice, the harmonics are not radiated isotropically. In the harmonics radiation measurement in the electromagnetic compatibility chamber, a receiving antenna is used to measure the radiated harmonics field in some distance, the total harmonics radiation is calculated based on the assumption that the harmonics are radiated isotropically. The maximum value of the harmonics is taken after several measurements with different positions of the antenna under test. Thus, it is logical to multiply P_{har} with the directivity of the radiator at the harmonics frequency.

Tab. 3.5 gives the comparison of the result from the model and the measurement for the tunable DVB-H antenna shown in Fig. 3.14. An EGSM coupler is constructed on the same printed circuit board. The tuning circuit of the DVB-H antenna is shown in Fig. 3.15. In measurement, a 33 dBm continuous wave signal is fed into the EGSM port, with the DVB-H port terminated with 50 Ω load.

Good agreements are only at some tuning voltages. The main reason is the inaccurate SPICE model of the varactor diode. For the nonlinear property of the varactor diode, a highly critical parameter is the junction

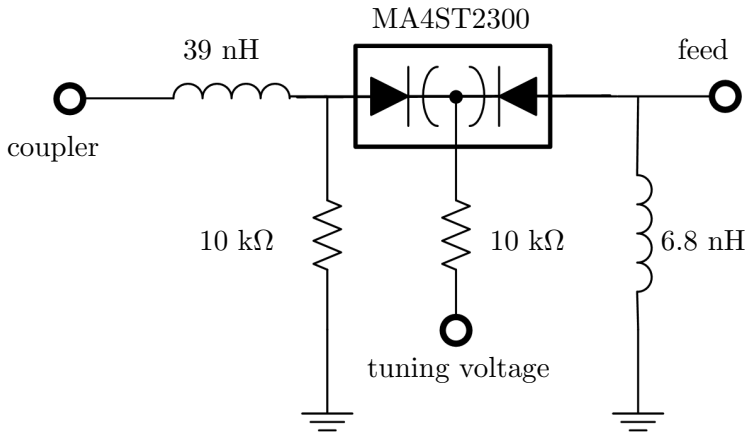

Figure 3.15: Schematic of the tunable matching circuit for the tunable DVB-H antenna shown in Fig. 3.14.

bias voltage / V	0.5	1.6	2.5	3.0	3.5
center frequency / MHz	470	550	650	680	710
measured 2nd harmonic / dBm	−55.1	−36.4	−30.3	−29.1	−28.6
modeled 2nd harmonic / dBm	−77.5	−54.6	−39.2	−33.1	−28.8
measured 3rd harmonic / dBm	−53.7	−31.1	−33.2	−43.1	−35.1
modeled 3rd harmonic / dBm	−59.3	−27.3	−11.1	−6.2	−3.1

Table 3.5: The comparison of the measured harmonics radiation levels for the tunable DVB-H antenna together with EGSM antenna on a 110 mm ×55 mm PCB (shown in Fig. 3.14) and the estimated harmonics radiation level from the model.

grading coefficient, which is modeled as a value independent of the control voltage in SPICE. However, in reality the value of the junction grading coefficient changes with the control voltage ([32], page 121).

3.5 Design of the tunable matching circuits

3.5.1 Estimating the number of tuning states

The design of a tunable antenna starts with designing a non-tunable prototype antenna, which should fulfill all the mechanical requirements: volume, size and shape of the printed circuit board, port definition, etc. The antenna should cover part of the target band with required maximum return loss and efficiency. The bandwidth of the non-tunable prototype antenna is denoted as B_{nt}. All the applications define the lower limit of the instantaneous bandwidth B_{inst} of the tunable antenna. For GSM and DVB-H, B_{inst}

should be larger than the bandwidth of one channel. Smaller B_{inst} leads to more tuning states which results in lossier, more non-linear and more complicated tuning circuit. It should also be kept in mind that, all the practical tuning devices are lossy. RF current flows through the tuning elements and causes loss, (otherwise the tuning elements are isolated, and the antenna is not tunable). In principle, the efficiency of the antenna goes down.

The instantaneous bandwidth B_{inst} of the tunable antenna in most cases is not larger than the bandwidth of non-tunable prototype antenna B_{nt} at the same center frequency, due to parasitics of the tuning devices. The minimum number of tuning states N required to cover the total bandwidth B_{total} can be estimated by

$$N = \frac{B_{\text{total}}}{B_{\text{nt}}}. \tag{3.10}$$

If the tunable antenna is constructed by a switch, the switch should be Single-Pole-N-Throw or Double-Pole-($N/2$)-Throw.

It should be noted that, in practice B_{nt} often varies with the center frequency, e.g. Tab. 3.3. For the mobile antenna in lowbands (e.g. DVB-H, GSM 850 and GSM 900), the higher the operating frequency is, the higher coupling efficiency between the printed circuit board and the coupler is, and the larger the attainable bandwidth can be achieved.

From Tab. 3.3, a DVB-H tunable antenna based on the non-tunable prototype antenna shown in Fig. 3.4 with the matching circuit shown in Fig. 3.8 should have $N \geq 9$ tuning states.

If the tunable antenna is implemented by one varactor diode, From the equation of the resonance frequency of L-C circuit

$$f_{\text{r}} = \frac{1}{2\pi\sqrt{L \cdot C}}, \tag{3.11}$$

the capacitance ratio r_{c} of the varactor diode should be

$$r_{\text{c}} \geq \left(\frac{f_{\text{c,high}}}{f_{\text{c,low}}}\right)^2, \tag{3.12}$$

with $f_{\text{c,high}}$ and $f_{\text{c,low}}$ the center frequencies of the highest and lowest instantaneous band respectively. For DVB-H, $r_{\text{c}} \geq 2.3$.

3.5.2 Ways of introducing tuning devices

After the design of the non-tunable prototype antenna, tuning devices should be introduced to make the antenna electrically tunable. Introducing tuning devices is the key part of the tunable antenna design. The introduced tuning devices should make the attainable band shift over frequency. The instantaneous bandwidth (B_{inst}) should be kept close to that of the non-tunable prototype antenna B_{nt} at the same center frequency.

In designing the non-tunable prototype antenna, especially during the process to control the center frequency f_c of the attainable band, some parts of the antenna whose changes affect (almost) only f_c can be found. The most commonly used tuning devices are varactor diodes, switches, control-FETs, etc. The control-FET (e.g. AF002C4-39 and AF002C1-39 from Skyworks Solutions, Inc.) are different from the normal semiconductor switches like the single-pole-single-throw switches. The control-FET have three pins, one control pin, two signal pins corresponding to the signal path, like an ideal switch. The impedance between the two signal pins can be described with a resistance when it is "on", and a capacitance when it is "off". For the semiconductor switches, they have at least six pins, and the output pin is normally either grounded or connected to an internal 50 Ω load to improve the isolation when this pin is not selected. They are normally described by their S-parameters.

The electrical tunability of the antenna components can be implemented by the following ways:

- Changing the electrical length of the transmission line can be implemented by using a control-FET to shunt part of the transmission line (Fig. 3.16a), or using two switches to select among the transmission lines of different lengths (Fig. 3.16b). It can also be approximated by inserting varactor diode(s) in the transmission line (Fig. 3.16c). Here we can distinguish three ways of solution.
  - Using a control-FET can achieve a very large frequency tuning range. Its disadvantage is that when the control-FET is in the "off" state, due to the "off"-state capacitance between the two signal pins of the control-FET, the loop formed by the shunted transmission line and the control-FET may resonate in or near the operating band, which causes big loss.
  - Using two switches has the advantages of a very large frequency tuning range, the best linearity among all the three ways. Its disadvantages are the most complicated layout and the large required printed circuit board area due to the transmission lines of various lengths.
  - Inserting varactor diode(s) has the advantage of continuous tunability and simple circuitry. Its disadvantage is the limited frequency tuning range due to the finite capacitance ratio of the available varactor diodes.
- To change the capacitive coupling between the coupler and the printed circuit board which is related to the distance between them, varactor diode(s) can be inserted between the coupler and the printed circuit board.

- The tunability of an inductive reactance with the maximum of $X_{\max}$ to achieve the operating band centered at ω_1, and the minimum of $X_{\min}$ for ω_2 can be achieved by three different ways.

  - An inductor $L_0 > X_{\max}/\omega_1$ is connected in series of a varactor diode with the maximum and minimum capacitance $C_{\max}$, $C_{\min}$ shown in Fig. 3.17a. From the circuit equations, the values of L_0, $C_{\max}$ and $C_{\min}$ should fulfill

$$\omega_1 L_0 - \frac{1}{\omega_1 C_{\max}} = X_{\max} \tag{3.13}$$

$$\omega_2 L_0 - \frac{1}{\omega_2 C_{\min}} = X_{\min}. \tag{3.14}$$

    This method has the advantage of the continuous tunability and a simple circuitry. Its disadvantage is the limited frequency tuning range due to the finite capacitance ratio of the available varactor diodes.

  - Two inductors L_1 and L_2 are connected in series with L_2 shunted by a control-FET. The values of L_1 and L_2 are

$$L_1 = \frac{X_{\min}}{\omega_2} \tag{3.15}$$

$$L_2 = \frac{X_{\max}}{\omega_1} - \frac{X_{\min}}{\omega_2}. \tag{3.16}$$

    More tuning states can be achieved by a series of several inductors which are shunted by control-FETs, shown in Fig. 3.17b. The drawback of this solution is similar to that of the circuit shown in Fig. 3.16a since the loop formed by the shunted inductor and the control-FET may resonate in or near the operating band. This yield a considerable loss.

  - As shown in Fig. 3.17c, inductors of various values are selected via two switches. This structure has the advantages of very large frequency tuning range, the highest linearity among all these three solutions. Its disadvantages are the complicated layout and large required printed circuit board area for the inductors.

- A tunable capacitor can be implemented by varactor diode(s) or by capacitors in combination with switches or control-FETs.

- To switch between different sets of circuit, e.g. two matching networks for two frequency bands, two switches can be used to select the signal flow-path.

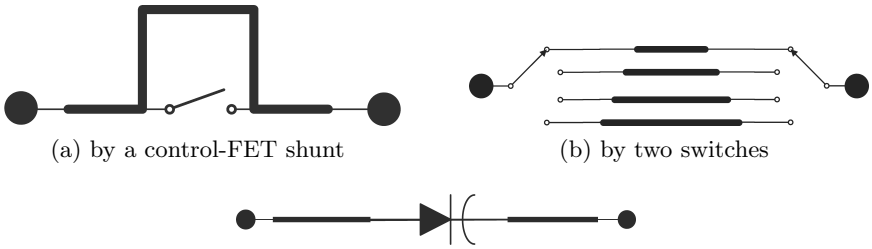

(a) by a control-FET shunt (b) by two switches

(c) by inserting varactor diode

Figure 3.16: Realizations of variable length transmission lines.

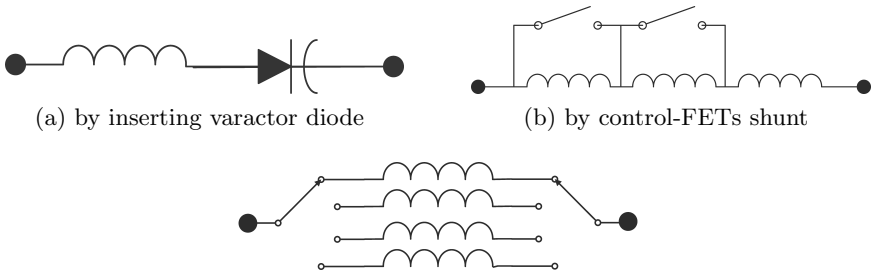

(a) by inserting varactor diode (b) by control-FETs shunt

(c) by two switches

Figure 3.17: Realizations of variable inductive reactances.

- To change the position of the junction, e.g. to change the position of the feed point, one switch can be used. It should be noted that, for most switches, the output pin is either grounded (reflective type) or connected to a 50 Ω internal load (non-reflective type) when it is "off". Only a few switches present open pins, e.g. the single-pole-double-throw switch HMC226/226E available from Hittite Microwave Corporation.

- Electromechanical solutions can be realized by using MEMS devices [33], micromotors, piezo element, or devices based on electroactive polymers or electrodynamic materials.

3.5.3 Devices selection

Basic considerations

After choosing the way of introducing tuning devices, the next step is selecting the proper devices from those available in the market. At this point, the basic requirements on the devices are known: the number of states of the switches, the $C_{\max}$ and $C_{\min}$ of the varactor diodes, the number of control-FETs, etc. Apart from that, other important requirements are

- Control voltage: Switches controlled by a higher control voltage can handle higher power and show better linearity. For varactor diodes, higher maximum bias voltage leads to larger capacitance ratio. On the other hand, to obtain a control voltage over 3 V in a mobile phone is difficult.

- Tuning speed: Some applications do not require high tuning speed. For example, as GSM 850 and EGSM 900 exist in different countries, the tunable antenna which is tunable between GSM 850 and EGSM 900 does not need high tuning speed. The tuning time can be milliseconds, or seconds. On the contrary, for channel-to-channel tuning, e.g. for DVB-H tunable antenna, the tuning speed should be in the range of microsecond. In this case, mechanical ways including MEMS are not preferred.

- Device lifetime: Some applications require tuning frequently, e.g. DVB-H channel-to-channel tuning, the lifetime should be over one hundred thousand. On the contrary, for some applications of infrequent tuning like those between GSM 850 and GSM 900, the device with a lifetime of thousands is acceptable.

- DC (bias) power consumption: In mobile applications, one important issue is the power consumption. As the DC power consumed by the tuning devices is provided by the battery with limited stored energy, low DC power consumption is required for a long operating time. That is the reason why switches based on PIN diode are not preferred.

- Discrete or continuous tuning: The discrete tuning stages provided by switch and control-FET have higher accuracy over that of the varactor diodes. However, in some cases, continuous tuning is preferred.

- Layout complexity and mounting: The layouts of switches are more complicated than those of the varactor diodes and the control-FETs. Mounting techniques are different for different packages which should be taken into account.

- Price.

Solid state devices

The RF properties of solid state devices are referenced in [34] [35]. This section is a summary of the properties of the tuning devices applicable in mobile applications.

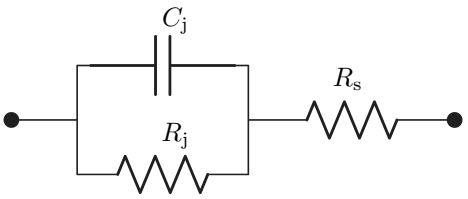

Figure 3.18: The equivalent circuit model for a varactor diode.

Varactor diodes [34]

A varactor diode is a semiconductor device with variable RF capacitance. Its variable-capacitance characteristics comes from the change of the diode depletion layer capacitance with the applied DC voltage.

The equivalent circuit model for a varactor diode is shown in Fig. 3.18, C_j and R_j are the depletion layer capacitance and junction resistance respectively, and R_s denotes the series resistance of the diode.

The depletion layer capacitance is

$$C_j = \frac{C_0}{(1 - V/V_0)^\gamma}, \tag{3.17}$$

with γ the exponent related to the doping profile, C_0 the zero-bias capacitance and V_0 the contact potential determined by the doping concentrations. For reverse bias the junction resistance R_j is generally high (e.g., tens of megaohms) and can be ignored. As an indicator of the efficiency, the quality factor of the varactor is defined by

$$Q_V = \frac{\omega C_j R_j}{1 + \omega^2 C_j^2 R_j R_s} \approx \frac{1}{\omega C_j R_s} \tag{3.18}$$

Generally, GaAs varactors have higher Q_V values than Si devices and are preferred in many high-efficiency and low-noise applications. An exception is in the low-phase-noise applications. The GaAs devices suffer from high baseband $1/f$ noise due to surface states, deep levels and other trapping effects. The Si devices, however, have the advantage of native oxide passivation that significantly reduces the low-frequency $1/f$ noise. In general, Si devices have a $1/f$ spectrum that is about 10∼20 dB lower in magnitude compared to that from GaAs devices. The $1/f$ corner frequencies where the $1/f$ effects can no longer be seen are in the hundreds of kilohertz range for Si devices and in the hundreds of megahertz for GaAs devices.

The capacitance variation of the varactor with the DC voltage as indicated in Equ. 3.17 depends on the exponent γ. For devices with abrupt doping profiles $\gamma = \frac{1}{2}$, for those with linearly graded profiles $\gamma = \frac{1}{3}$, and for hyperabrupt profiles $\gamma = 1 \sim 5$.

For a varactor diode, a series capacitor is often connected to increase the power efficiency as shown in Fig. 3.19, the quality factor of the series of a varactor and a capacitor

$$Q'_{\mathrm{S}} = Q_{\mathrm{V}} \frac{r_{\mathrm{c}} - 1}{r'_{\mathrm{c}} - 1} \tag{3.19}$$

should be compared, with r_{c} the capacitance ratio of the varactor diode, r'_{c} the required capacitance ratio in the tunable antenna design, and Q_{V} the quality factor of the varactor diode in the operating band. The varactor diode with the highest Q'_{S} is selected. Connecting the varactor diode in parallel with a capacitor shown in Fig 3.20 can increase the efficiency too, however, higher quality factor can be achieved by the series structure, which is discussed later.

Semiconductor switches [34]

For the design of control circuits, GaAs MESFETs are operated under two different modes: active and passive. In the active mode, single- or double-gate MESFETs are used as three-terminal active devices. In the passive mode of operation, MESFETs are used as passive two-terminal devices, with the gate terminal acting as a port for the control. The RF connections are made to the drain and the source terminals only, and the gate terminal looks into an open circuit for the RF signal. The RF impedance between the drain and the source terminals depends on the DC control voltage at the gate terminal. For switching applications, low-impedance and high-impedance states are obtained by making the gate voltage equal to zero and by using a gate voltage greater than the pinchoff voltage, respectively.

In the low-impedance state, the channel presents a resistive path to the RF current between the drain and the source. The typical value of R_{on} for a $1 \times 1000\,\mu\mathrm{m}^2$ gate MESFET suitable for X-band operation is about 2.5 Ω at around 10 GHz. Use self-aligned gate technology to reduce the value of R_{on} have been reported [36].

For the high-impedance state of MESFETs operating in the passive mode, as the channel is now pinched off, the capacitance of the depletion layer(C_{g}) appears in series between the source and drain terminals. Also in this case, the capacitance C_{sd} (and the leakage resistance r_{d}) between the source and the drain terminals needs to be incorporated in the equivalent circuit. For a $1 \times 1000\,\mu\mathrm{m}^2$ gate MESFET operating at 10 GHz, typical values of the various elements are $C_{\mathrm{sd}} \approx 0.25\,\mathrm{pF}$, $r_{\mathrm{d}} \approx 3\,\mathrm{k}\Omega$, and $C_{\mathrm{g}} \approx 0.2\,\mathrm{pF}$. As r_{g} is much smaller than the reactance of C_{g}, the equivalent circuit can be simplified into R_{off} in parallel with C_{off}, where

$$\begin{aligned} C_{\mathrm{off}} &= C_{\mathrm{sd}} + \frac{C_{\mathrm{g}}}{2} \\ R_{\mathrm{off}} &= \frac{2r_{\mathrm{d}}}{2 + r_{\mathrm{d}}\omega^2 C_{\mathrm{g}}^2 r_{\mathrm{g}}}. \end{aligned} \tag{3.20}$$

Typical values for C_{off} and R_{off} for $1 \times 1000\,\mu\text{m}^2$ gate devices at 10 GHz about 0.2 pF and 2 kΩ, respectively. It may be noted that R_{off} is now a function of the operating frequency ω.

In the tunable antenna applications, this C_{off} may introduced unwanted resonance. A rule of thumb is making the resonance frequency far from our operating frequency.

YIG resonators [34]

The YIG resonator is a ferrite resonator with high quality factor that can be tuned over a wide frequency range by varying the biasing DC magnetic field. Its high performance and convenient size make it an excellent choice in a large number of commercial and military applications. A YIG resonator makes use of the ferromagnetic resonance that occurs when a small magnetic microwave field is applied perpendicular to a static magnetic field.[34] Depending on the material composition, size and applied field, resonance frequencies between 500 MHz and 50 GHz can be achieved [37].

Design of the magnetic circuit forms an important aspect of any YIG device design due to the fact that it is the value of the magnetic field that determines the resonance frequency of the YIG resonator. The YIG magnetic tuning circuits dissipate large DC power. Typically it is about 5 W at 12 GHz and the tuning sensitivity lies between 15 and 25 MHz/mA [34]. In addition to the standard magnetic structure, permanent magnetic structures are also used in some applications. Permanent magnets requires smaller DC power which is commonly used for narrow-band applications offering significant reduction of size and power dissipation [34].

MEMS [34]

A microelectromechanical system (MEMS) integrates electrical and mechanical functions in a single component using microfabrication and micromachining technology similar to the semiconductor integrated circuit processing. MEMS technology enables the integration of microelectronics with the actuation, sensing and control capabilities of microsensors and microactuators. Typical sizes for MEMS components range from micrometers to millimeters. [34]

MEMS devices employed in radio-frequency applications are termed RF MEMS. They feature low insertion loss, high isolation, high quality factor, small size and low power consumption.[34]

Details about MEMS devices fabrication and assembly are available in literatures [34] [35] [38].

For tunable antenna application, two type of MEMS devices are of most interest: RF MEMS variable capacitor (Varicap) and RF MEMS switch.

Performance and characteristics	Electromagnetic Relays	Semiconductor Switches		RF MEMS Switches
		RF	Microwave	
Insertion loss	Low	Moderate	High	Low
Isolation	High	High	Moderate	High
Switching speed	Low	High	High	Low
DC Power	High	Moderate	Moderate	Low
Linearity	High	Low	Low	High
Operating temperature range	High	Low	Low	High
Device Density	Low	High	High	High
Reliability	High	High	Moderate	Moderate
Cost	High	Low	Moderate	Low
Ease of integration	Low	Moderate	Moderate	Moderate

Table 3.6: Comparison of MEMS switches with other switches, from [34].

MEMS switches

An RF MEMS switch consists of RF electrodes that can be actuated to short or open an RF transmission line. The RF MEMS switches have the advantages of low insertion loss, high isolation and linearity. A qualitative comparison of MEMS switches with other switches is given in [34], and listed in Tab. 3.6.

For example, TT712-68CSP is a Single-Pole-Double-Throw MEMS switch by TeraVicta, which features the following:

- Control voltage: 68 V
- Maximum insertion loss: 0.4 dB in the range from DC to 7 GHz
- Input IP3: 65 dBm
- Output 1 dB compression point: 47 dBm
- Switching speed: 70 μs
- RF hot life cycles: 100 millions

MEMS varicaps

The MEMS varicaps are widely used for their tuning functionality in RF communication circuit applications. In MEMS varicaps, the capacitance is changed by adjusting the physical dimensions of the device. In these capacitors, the dielectric layer used is usually air, which eliminates the majority of the dielectric losses and results in high quality factors. The MEMS varactors have been designed for analog and digital capacitance variations. In

analog designs, the capacitance value can be changed continuously, whereas in digital designs, the capacitance value is changed stepwise.

For example, WSC001L is a tunable low-voltage RF MEMS varicap with digital design provided by wiSpry. It features the follow:

- Minimum capacitance: 0.1 pF
- Maximum capacitance: 0.975 pF
- Quality factor: 100 at 2 GHz at the state of 0.975 pF
- Maximum RF power: 1.25 W
- Switching time: 50 μs

Mechanical tuning methods

Mechanical ways by using piezo elements, electroactive polymers and electrodynamic materials offer large tuning range and high linearity. Normally, they feature low speed, and short life cycle.

Trade-offs between the tuning range and efficiency

In reality, all the tuning elements are lossy due to the finite channel conductance of the FETs, the junction resistance of the varactor diodes, the parasitics of the packages, etc. If the antenna is required to be tunable, part of the current must flow through the tuning elements and loss is generated.

In practice, there exists a trade-off between the obtained large tuning range and the low antenna efficiency degradation. If the tunable antenna is constructed based on switches and control-FETs, the introduced loss can be estimated by their insertion loss stated in the data sheets. In most cases, the more states a switch has, the higher its insertion loss is. For a control-FET, as it has only two states, achieving large tuning range will require more control-FET introduced in the antenna, thus more loss is generated.

As an example, Tab. 3.7 lists the insertion loss of some switches for planar circuits available in the market. The switches based on PIN diode are not included due to the high bias current which is impractical in mobile applications. It should be noted that, in chip selection, more specifications than those in Tab. 3.7 should be taken into account, e.g. frequency range, maximum input RF power, state of the pin when it is "off", etc.

The loss of a varactor diode can be characterized by its junction capacitance and quality factor. Connecting varactor in series or parallel with a capacitor can reduce the generated loss by dividing the RF current or voltage, with the sacrifice of the tuning range. The reduction of the tuning range can be estimated in the following.

part number	company	description	insertion loss (dB)	package
MASW-007107-0	M/A-COM	pHEMT SPDT	0.5 at 2 GHz	PQFN
MASW-007221-0	M/A-COM	GaAs SPDT	0.35 at 1 GHz	SC-70
MASW-007587-0	M/A-COM	pHEMT DPDT	0.6 at 1 GHz	PQFN
MASW-007588-0	M/A-COM	pHEMT SPDT	0.7 at 2.4 GHz	PQFN
MASW-007813-0	M/A-COM	pHEMT SP4T	0.7 at 1 GHz	PQFN
MASW-007935-0	M/A-COM	pHEMT SPDT	0.5 at 1 GHz	SOT-26
MASW-008330-0	M/A-COM	pHEMT SP3T	0.3 at 1 GHz	PDFN
MASW-008566-0	M/A-COM	pHEMT SP4T	0.65 at 1 GHz	PQFN
MASWCC0006	M/A-COM	pHEMT SP6T	1.5 at 1 GHz	PQFN
MASWSS0028	M/A-COM	pHEMT SP3T	0.3 at 1 GHz	PQFN
MASWSS0118	M/A-COM	pHEMT SP4T	0.65 at 1 GHz	PQFN

Table 3.7: Insertion loss of some switches available in the market.

Fig. 3.19 shows a varactor connected with an ideal series capacitor C_s. The varactor diode is modeled as a series connection of an ideal varactor C_V and resistor R_s. The quality factor Q_V of the varactor diode at frequency ω is

$$Q_\mathrm{V} = \frac{1}{\omega C_\mathrm{V} R_\mathrm{s}}. \tag{3.21}$$

The varactor diode has the capacitance ratio of $r_\mathrm{c} = C_\mathrm{max}/C_\mathrm{min}$. The quality factor of the whole circuit is

$$Q'_\mathrm{S} = \frac{C_\mathrm{s} + C_\mathrm{V}}{\omega C_\mathrm{s} C_\mathrm{V} R_\mathrm{s}}, \tag{3.22}$$

and the capacitance ratio

$$r'_\mathrm{c} = \frac{\frac{C_\mathrm{s} C_\mathrm{max}}{C_\mathrm{s}+C_\mathrm{max}}}{\frac{C_\mathrm{s} C_\mathrm{min}}{C_\mathrm{s}+C_\mathrm{min}}} = \frac{r_\mathrm{c} - 1}{1 + \frac{C_\mathrm{max}}{C_\mathrm{s}}} + 1. \tag{3.23}$$

Q_V, Q'_S, r_c and r'_c can be related by

$$\frac{Q'_\mathrm{S}}{Q_\mathrm{V}} = \frac{r_\mathrm{c} - 1}{r'_\mathrm{c} - 1}. \tag{3.24}$$

For parallel connection of varactor and capacitor C_P shown in Fig. 3.20, the relation is

$$\frac{Q'_\parallel}{Q_\mathrm{V}} = \frac{r'_\mathrm{c}}{r_\mathrm{c}} \left(\frac{r_\mathrm{c} - 1}{r'_\mathrm{c} - 1}\right). \tag{3.25}$$

Both Equ. 3.24 and 3.25 reach infinity when $r'_\mathrm{c} = 1$, corresponding to $C_\mathrm{s} = 0$ or $C_\mathrm{P} = +\infty$; and 1 when $r'_\mathrm{c} = r_\mathrm{c}$. For the same $r'_\mathrm{c}/r_\mathrm{c}$ ratio, $Q'_\mathrm{S}/Q'_\parallel = r_\mathrm{c}/r'_\mathrm{c} \geq 1$, so series structure is preferred to the parallel one.

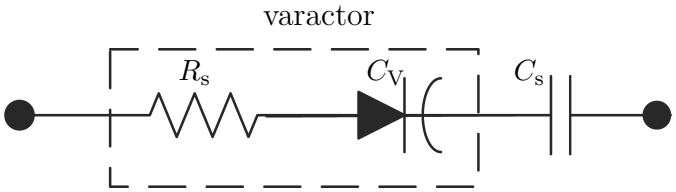

Figure 3.19: Schematic of the series of a varactor and a capacitor.

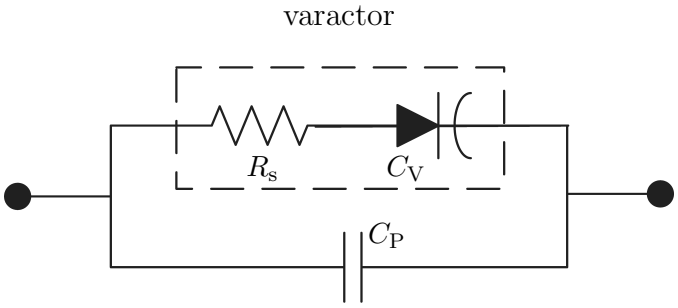

Figure 3.20: Schematic of the parallel varactor and capacitor.

Trade-offs between the tuning range and linearity

The switches with high values of IP2 and IP3 are preferred. As an example, Tab. 3.8 listed the IP3 values of some switches available in the market. Higher value of IP3 can be achieved sometimes by increasing the control voltage.

Theoretically, anti-series varactor pair (ASVP) constructed by two identical varactors can fully get rid of the even-order intermodulation and second-order harmonics distortion. Some device companies provide ASVPs in single chip packages, e.g. MA4ST2300CK by M/A-COM. [39] concluded that the third-order intermodulation and the third-order harmonics distortions of the ASVP can be greatly suppressed without dependence on the bias voltage when two single varactors in the ASVP have ideal abrupt p-n junctions with $\gamma = 0.5$, or its C-V characteristics fulfills the following relation

$$C_V(V) = \frac{A}{\sqrt{B - V}}, \tag{3.26}$$

where A and B are arbitrary constants.

In reality, γ changes with the bias voltage of the varactor [32], and sometimes the hyperabrupt varactors are chosen for their large capacitance ratio. Methods to suppress the harmonics are proposed in the following section.

part number	company	description	linearity	package
MASW-007107-0	M/A-COM	pHEMT SPDT	IP3=57 dBm 2.4 GHz, 3 V	PQFN
MASW-007221-0	M/A-COM	GaAs SPDT	IP3=52 dBm 900 MHz, 3 V	SC-70
MASW-007587-0	M/A-COM	pHEMT DPDT	IP3=57.5 dBm 2.4 GHz, 3 V	PQFN
MASW-007588-0	M/A-COM	pHEMT SPDT	IP3=57 dBm 2.4 GHz, 3 V	PQFN
MASW-007813-0	M/A-COM	pHEMT SP4T	IP3=58 dBm 2.75 V	PQFN
MASW-007935-0	M/A-COM	pHEMT SPDT	IP3=50 dBm 900 MHz, 2.7 V	SOT-26
MASW-008330-0	M/A-COM	pHEMT SP3T	IP3=50 dBm 2.5 V	PDFN
MASW-008566-0	M/A-COM	pHEMT SP4T	IP3=57 dBm 2.5 V	PQFN
MASWCC0006	M/A-COM	pHEMT SP6T	IP3=40 dBm	PQFN
MASWSS0028	M/A-COM	pHEMT SP3T	IP3=50 dBm 2.5 V	PQFN
MASWSS0118	M/A-COM	pHEMT SP4T	IP3=57 dBm 2.5 V	PQFN

Table 3.8: Linearity comparison of some switches available in the market.

3.6 Approaches to improve the isolation

3.6.1 Low-band ports isolation

In practice, mobile services with their operating band close to each other are required to be supported by one single mobile. A multiplexer constructed with filters is put between the transceivers and the antenna(s) to separate the signals of different services. For example, due to the narrow intermediate band between EGSM 900 (880 MHz - 960 MHz) and DVB-H (470 MHz - 702 MHz), the multiplexer should be constructed by high-order filters to provide enough suppression on the EGSM transmitter (uplink) signal before it enters the DVB-H receiver. Thus, the insertion loss of the multiplexer is quite high.

It is preferred that the antenna(s) can provide some separation between the signals before they enter the multiplexer. A multi-port antenna with each port corresponding to one individual service band can provide signal separation to some extent.

For the capacitive coupler working in lowband, as stated before, the coupler need to be put in front of the short edge of the printed circuit board. To suppress the direct coupling between the two couplers, the two couplers need to be put at the opposite ends of the printed circuit board. Thus, the signal A from port A couples first from the corresponding coupler to the printed circuit board, then couples to coupler B from the printed circuit board [21]. These two coupling processes provide attenuation of the signal A before it enters port B.

Fig. 3.21 shows a two-port mobile antenna. An EGSM 900 coupler and a tunable DVB-H coupler are put at the opposite ends of the 110 mm $\times$55 mm printed circuit board. The length of the printed circuit board is shorter than a half wavelength. Both the DVB-H port and GSM port are matched to 50 Ω with the maximum $|\Gamma|$ of -7 dB. Despite the fact that EGSM and DVB-H bands are close in frequency, the achieved isolation in EGSM band between the ports is over 16 dB, shown in Fig. 3.22.

For lowband applications, e.g. GSM 850, 900 and DVB-H, as they all utilize the chassis mode with current flowing along the longer side of the printed circuit board to achieve small reflection magnitude, the infinite isolation between the ports can not be obtained.

3.6.2 Isolate the tuning device from the nearby TX signal

In some applications, e.g. DVB-H, the high-power transmitting (TX) signals from the transmitters in the mobile terminals cause non-linear distortions and intermodulations on the tuning devices. For lowband applications, considering an EGSM TX signal with the peak power of 33 dBm, and a port-to-port isolation of roughly 10 to 20 dB, approximately another 20 dB TX

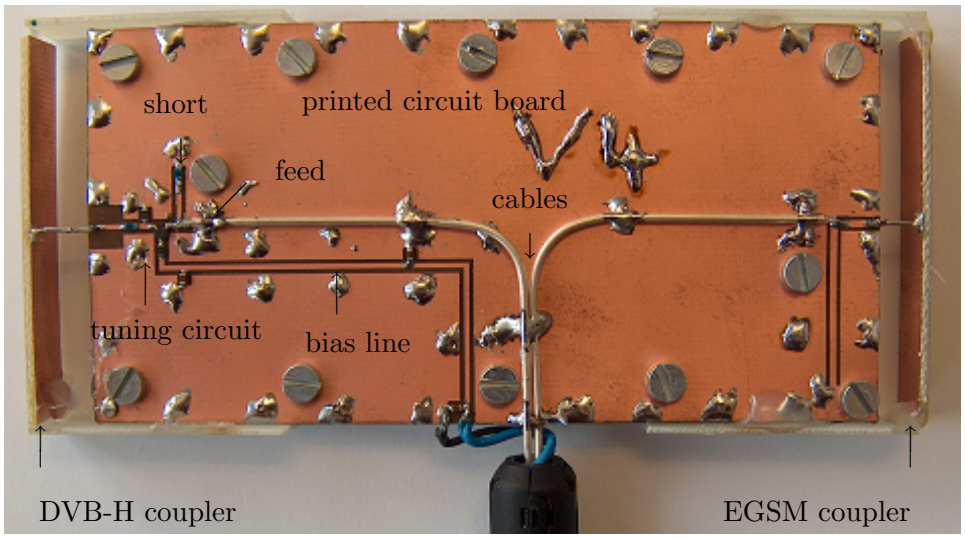

Figure 3.21: Photo of the tunable DVB-H antenna, together with an EGSM antenna attached to a 110 mm ×55 mm printed circuit board.

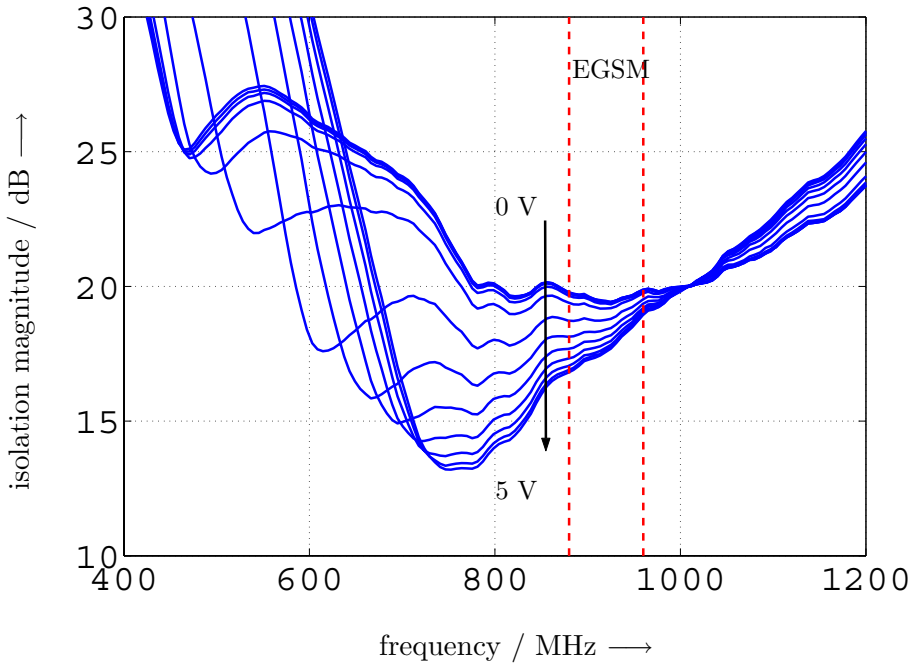

Figure 3.22: Measured isolation between the DVB-H and EGSM ports of the antenna shown in Fig. 3.21 over frequency for the tuning voltage in the range from 0 to 5 V.

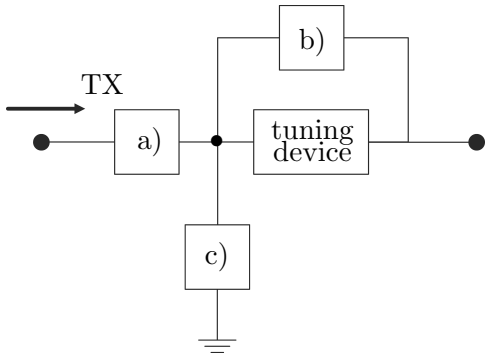

Figure 3.23: The schematic of possible modules to isolate the tuning device from the TX signal, with a) the module to block the TX, b) the module to shunt TX current, c) the module to divert the TX current to ground.

suppression is needed for the tuning devices. Possible modules which suppress the TX-signal are shown in Fig. 3.23, with

- Module a) the module to block the TX.
- Module b) the module to shunt TX current.
- Module c) the module to divert the TX current to ground.

The module a) b) and c) are constructed by inductors and capacitors. For narrow band TX signals, they can be a simple resonant LC circuit, and for broadband TX signals, they can be realized by filters.

Fig. 3.24 shows a mobile terminal with two couplers. One EGSM 900 coupler and a DVB-H tunable coupler. A third-order bandstop filter with the attenuation of more than 40 dB in EGSM-TX is placed between the DVB-H coupler and the tuning varactor diodes to block the EGSM-TX.

3.7 Approaches to suppress the harmonics

The harmonics of the tunable antenna can be suppressed by introducing "open"s or "short"s at the tuning devices at the harmonics frequency, which block or shunt the harmonics current. "Short" and "open" can be realized by resonant series and parallel LC circuits respectively. If a series LC resonates at the harmonics frequency, it is capacitive at the fundamental frequency. If a parallel LC resonates at the harmonics frequency, it is inductive at the fundamental. And these capacitive or inductive parts may reduce the antenna tuning range. Structures which are "invisible" at the fundamental are preferred.

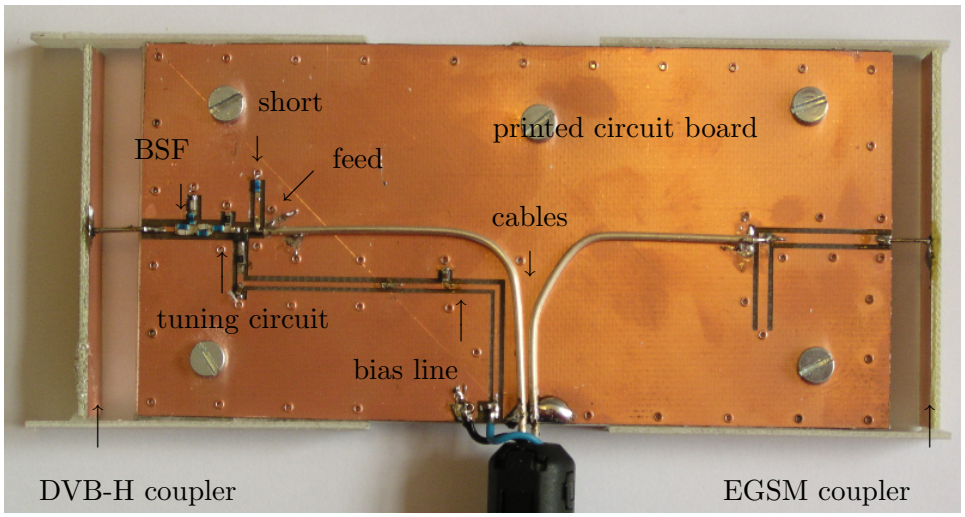

Figure 3.24: Photo of the tunable DVB-H antenna, together with an EGSM antenna attached to a 110 mm ×55 mm printed circuit board. A bandstop filter(BSF) is put between the tuning circuit and the coupler to isolate the tuning devices from the EGSM TX signal.

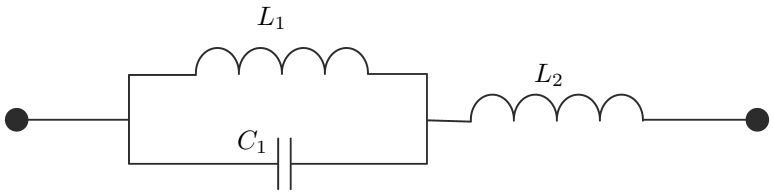

Figure 3.25: Schematic of the type 1 harmonics suppression circuit.

In this section, two types of passive circuit structures are developed. The circuit type 1 presents "open" at the fundamental frequency ω_0, and "short" at the higher frequency (harmonics frequency). The circuit type 2 presents "short" at fundamental frequency, and "open" at higher frequency.

The circuit type 1

The circuit type 1 shown in Fig. 3.25 presents

@ ω_0	open
@ $t \cdot \omega_0$	short

at its terminal, with $t > 1$. Procedure to achieve the values of L_1, C_1 and L_2 is given below.

The impedance presents at the terminal is,

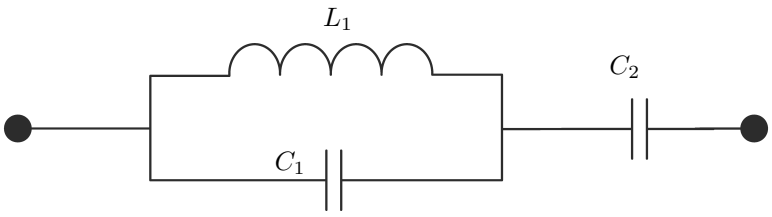

Figure 3.26: Schematic of the type 2 harmonics suppression circuit.

$$\begin{aligned} Z =& \mathrm{j}\omega L_2 + \frac{\mathrm{j}\omega L_1 \cdot \frac{1}{\mathrm{j}\omega C_1}}{\mathrm{j}\omega L_1 + \frac{1}{\mathrm{j}\omega C_1}} \\ =& \mathrm{j}\omega \cdot \frac{L_2 + L_1 - \omega^2 L_1 L_2 C_1}{1 - \omega^2 L_1 C_1} \end{aligned} \tag{3.27}$$

If C_1, L_1 and L_2 fulfill the following requirements,

$$\frac{1}{L_1 C_1} = \omega_0^2 \tag{3.28}$$

$$L_2 = \frac{L_1}{t^2 - 1}, \tag{3.29}$$

$Z = \mathrm{j} \cdot \infty$ (open) at ω_0 and $Z = 0$ (short) at $t \cdot \omega_0$.

The circuit type 2

The circuit type 2 given in Fig. 3.26 presents

@ ω_0	short
@ $t \cdot \omega_0$	open

at its terminal, with $t > 1$. Procedure to achieve the values of C_1, L_1 and C_2 is given below.

The impedance is,

$$\begin{aligned} Z =& \frac{1}{\mathrm{j}\omega C_2} + \frac{\mathrm{j}\omega L_1 \cdot \frac{1}{\mathrm{j}\omega C_1}}{\mathrm{j}\omega L_1 + \frac{1}{\mathrm{j}\omega C_1}} \\ =& \frac{1}{\mathrm{j}\omega C_2} + \frac{\mathrm{j}\omega L_1}{1 - \omega^2 L_1 C_1} \\ =& -\mathrm{j}\Big(\frac{1}{\omega C_2} - \frac{\omega L_1}{1 - \omega^2 L_1 C_1}\Big) \\ =& -\mathrm{j}\Big(\frac{1 - \omega^2 L_1 C_1 - \omega^2 L_1 C_2}{\omega C_2 (1 - \omega^2 L_1 C_1)}\Big). \end{aligned} \tag{3.30}$$

If L_1, C_1 and C_2 fulfill

$$\frac{1}{L_1 C_1} = (t \cdot \omega_0)^2 \tag{3.31}$$

$$C_2 = C_1(t^2 - 1), \tag{3.32}$$

$Z = 0$ at ω_0 (short), and $Z = \mathrm{j} \cdot \infty$ at $t \cdot \omega_0$(open).

Chapter 4

Performance Metrics and Measurement Procedures

4.1 Limitations of the standardized measurement methods

The standardized non-linearity measurement methods of the mobile RF frontend assume that the antenna is linear and the non-linear effects are caused by the transmitter and the power amplifier. The non-linearities are measured at the output port of the power amplifier.

This assumption is true for all the non-tunable passive antennas. For the tunable antennas, as the non-linear tuning devices are introduced, the antenna becomes non-linear. The high-power signal from the power amplifier will be distorted by the tunable antenna and radiated. Due to the neglect of the tunable antennas' non-linearity, the standardized measurement methods are inaccurate.

4.2 Measurements of the radiated spectrum

Emission mask and intermodulation measurements

Both the emission mask measurement and the third-order intermodulation measurement are performed in the baseband.

The emission mask measurement set-up is shown in Fig. 4.1. A continuous-wave (CW) standardized signal (e.g. EGSM TX) is generated by a signal generator and amplified by a power amplifier (PA). A bandpass filter (BPF) or a lowpass filter (LPF) is inserted between the antenna under test (AUT) and the power amplifier to suppress the harmonics generated by the power amplifier. The antenna under test is connected to the output port of the filter. The incident power of the antenna under test should be calibrated to the level specified in the standards, e.g. 33 dBm for EGSM 900.

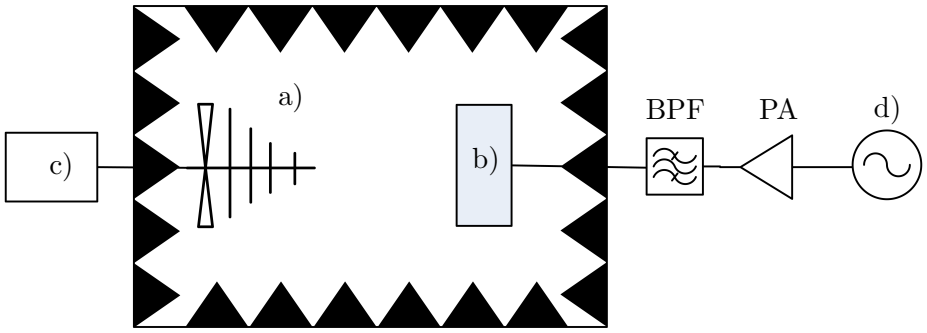

Figure 4.1: The experiment set-up for the emission mask measurement, with a) receiving antenna, b) antenna under test, c) spectrum analyzer, d) signal generator.

The spectrum of the radiated signal of the antenna under test is measured by a receiving antenna. This spectrum should be compared with the emission mask defined in the standard and the input spectrum of the antenna under test.

For the third-order intermodulation, two sinusoidal continuous-wave signals with their frequency close to each other are fed into the antenna under test. It should be noted that, the intermodulation of these two sinusoidal continuous-wave signals should not take place before they enter the antenna under test.

Spurious emission measurement

The measurement setup for the spurious emission is shown in Fig. 4.2. The signal is generated by a signal generator, amplified by a PA, filtered by a BPF or a LPF and fed into the antenna under test. The harmonics from the PA are suppressed by the BPF or LPF before the signal enters the antenna under test. The incident power of the antenna under test is calibrated to the specified value given in the standards. The radiated signals including baseband and harmonics are received by the receiving antenna. A bandstop filter (BSF or notch filter) is put after the receiving antenna to attenuate the baseband signal so as to improve the sensitivity of this measurement. The received harmonics are amplified by a low-noise amplifier (LNA) and measured by an EMI receiver. The total radiated harmonics power is calculated based on the assumption that the harmonics is radiated isotropically.

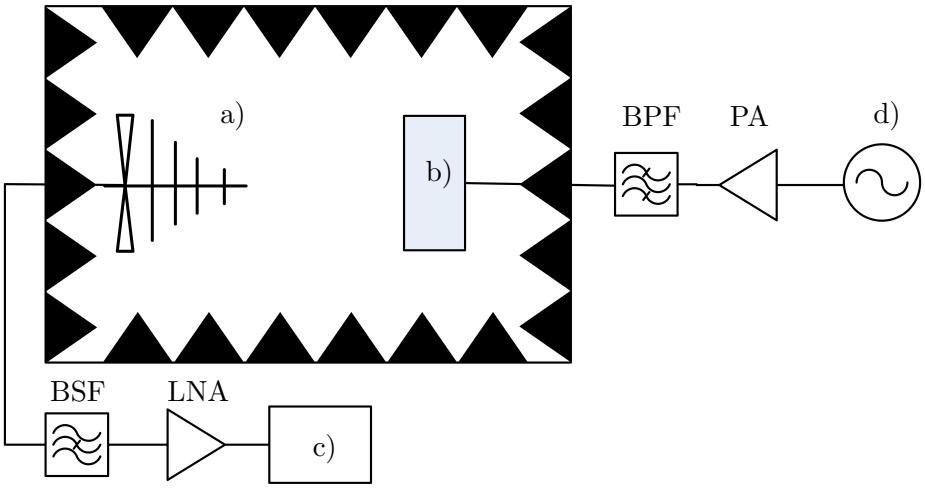

Figure 4.2: The experiment set-up for the spurious emission measurement, with a) receiving antenna, b) antenna under test, c) EMI receiver, d) signal generator.

4.3 Blocker resilience measurement

Background

Consider a tunable antenna connected to a transceiver, in the presence of a high-power TX (uplink) signal and an out-of-band RF interference (blocker) incident on the antenna from the air, their third-order intermodulation product (IM3) may drop in the receiving band of the antenna. As an example, Fig. 4.3 shows the measured spectrum at the port of a tunable DVB-H antenna with an EGSM coupler on the same printed circuit board shown in Fig. 5.7. In the presence of a 142 dB μV/m UHF blocker at 800 MHz, and a 33 dBm EGSM TX signal at 900 MHz, there is an -60 dBm IM3 component at 700 MHz which is in the DVB-H band.

In order not to interfer with the DVB-H signal reception, the level of the mixing product should be lower than the noise floor or several dB lower than the sensitivity of the receiver.

Measurement set-up

Fig. 4.4 shows the set-up for the blocker resilience measurement. The local TX signal is generated by a signal generator, amplified by a PA, filtered by a BPF to suppress the harmonics generated by PA and fed into the antenna under test through a multiplexer (MUX). The out-of-band interference (blocker) is generated by a second signal generator, amplified, filtered, and radiated by a transmitting antenna in the chamber. The IM3 from the

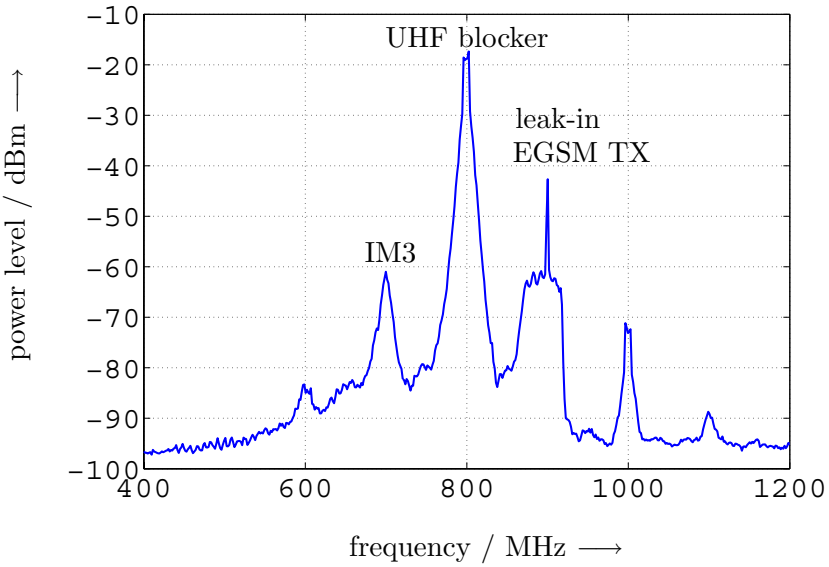

Figure 4.3: The output spectrum of one DVB-H tunable antenna with an EGSM coupler on the same printed circuit board shown in Fig. 5.7, in the presence of a 142 dB μV/m UHF blocker at 800 MHz and a 33 dBm EGSM TX (uplink) signal at 900 MHz.

antenna under test goes through the BSF and measured by the spectrum analyzer.

The purpose of the BSF put before the spectrum analyzer is to attenuate TX power leaked from the MUX. BSF is preferred to BPF due to the broadband IM3 when both the local TX signal and the blocker are not sinusoidal. For example, in practice, the IM3 of the local GSM TX and the out-of-band digital TV (with 8 MHz bandwidth) has the bandwidth over 15 MHz.

Proposed lower limit on the UHF blocker resilience

The main interference in UHF (Ultra High Frequency) band is DVB-T. The specification [17] assumes a maximum allowed input power to the DVB-T receiver of -18 dBm. We assume that the corresponding field strength of the incident signal also presents a limit for any UHF blocker signal which occurs in practical applications. An estimate for the field strength can be obtained by approximating the antenna factor of our tunable antenna by that of a 100 mm long dipole. According to [40], page 158, a value of 26.5dB/m for the antenna factor at 800 MHz is used. This approximation yields a maximum expected blocker field strength of 115.5 dB μV/m. To leave some tolerance margin, a minimum blocker strength of 120 dB μV/m was chosen as the criterion for the blocker resilience measurement.

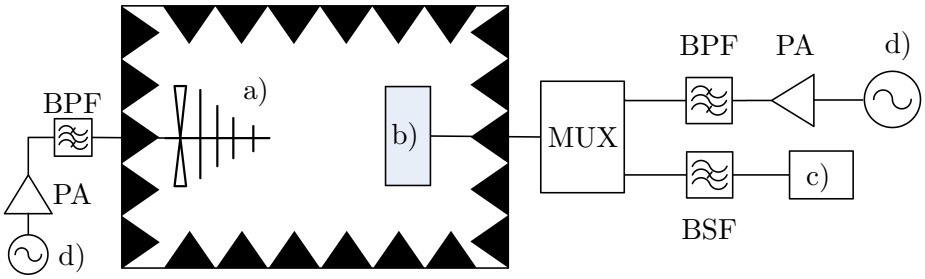

Figure 4.4: The experiment set-up for the blocker resilience measurement, with a) transmitting antenna, b) antenna under test (AUT), c) spectrum analyzer, d) signal generator.

Chapter 5

Demonstrator: DVB-H Tunable Antennas

5.1 Design consideration

The DVB-H radio access interface specifications are given in [17]. For a mobile phone supporting EGSM 900, the DVB-H antenna is required to cover the band from 470 MHz to 702 MHz (fractional bandwidth of 40%). The attainable bandwidth is limited physically depending on the size of mobile phone [2]. A somewhat tighter, more realistic limit was derived in [3]. For a DVB-H antenna mounted on a 110 mm $\times$55 mm printed circuit board, which is typical for a bar-type mobile phone, it predicts an upper bound on the fractional bandwidth of 34 % (for maximum 7 dB return loss). Since this bound is still optimistic compared to the practical results, use of a tunable antenna is an obvious choice to overcome the bandwidth limitation without adding volume. It should be noted that the instantaneous bandwidth of the tunable antenna must be larger than 8 MHz, which is the channel bandwidth of DVB-H.

A further issue for the DVB-H application in a mobile phone is the coexistence with EGSM. To attenuate the noise tail of the GSM transmitter in DVB-H band, a bandpass filter (BPF) is inserted instead of the usual lowpass filter between the EGSM transceiver and the antenna. Another BPF is placed before the DVB-H receiver to attenuate the leaking-in EGSM TX (880 - 915 MHz) signal below -25 dBm, which is the maximum allowed out-of-band unwanted signal level [17].

5.2 Non-tunable prototype antenna for DVB-H band

The non-tunable prototype antenna should fulfill all the mechanical requirements. In this work, a 110 mm $\times$55 mm rectangular printed circuit board is used as the chassis where the antenna is mounted. The antenna is designed

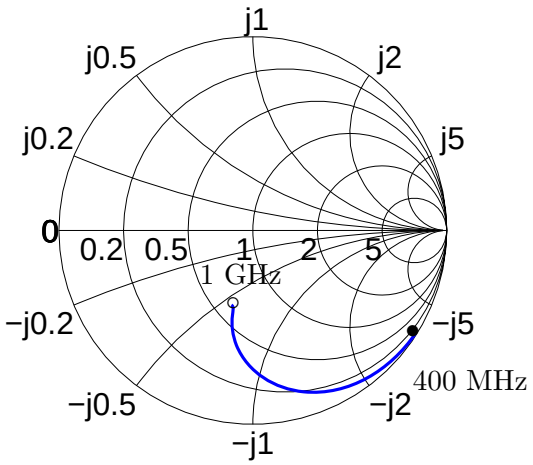

Figure 5.1: Simulated input impedance of the DVB-H coupler mounted on a 110 mm ×55 mm printed circuit board from 400 MHz to 1 GHz, by IE3D.

as a capacitive coupler in front of the short edge of the printed circuit board as shown in Fig. 3.3, with the width w and height h of the vertical board 55 mm and 10 mm respectively , and d the distance between the vertical board and the printed circuit board 8 mm. The simulated input impedance of the DVB-H coupler from 400 MHz to 1 GHz by IE3D is shown in Fig. 5.1.

Fig. 5.2 shows the schematic of the matching circuit used in the non-tunable prototype antenna to match the input impedance of the DVB-H coupler (Fig. 5.1) to a 50 Ω feed, with $L_2 = 7\,\text{nH}$ and L_1 from 40 nH to 10 nH to tune the resonance frequency f_c of the antenna from 470 MHz to 702 MHz. The optimum 7 dB bandwidth attained by the non-tunable prototype antenna is around 25 MHz with f_c of 470 MHz, and 60 MHz with f_c of 702 MHz. The bandwidth becomes larger when f_c approaches the resonance frequency of the printed circuit board (about 1 GHz) [21] [3]. It is estimated by the non-tunable prototype antenna that at least 7 tuning states are needed to cover the whole DVB-H band. In designing the non-tunable prototype antenna, L_1 is found to affect (almost) only f_c of the attainable band. The next task is to implement the tunable inductor.

5.3 Tunable DVB-H antenna

5.3.1 Antenna design

The structure with two single-pole-7-throw switches and 7 different inductors in between shown in Fig. 3.17c is not preferred, due to the high insertion

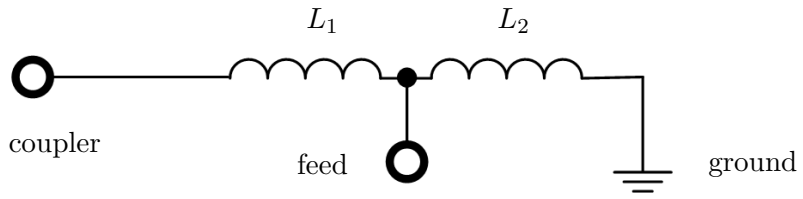

Figure 5.2: Schematic of the matching circuit for the non-tunable prototype DVB-H antenna.

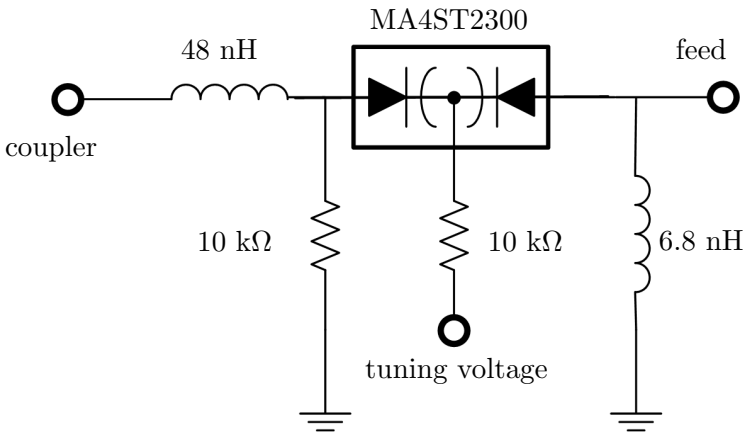

Figure 5.3: Schematic of the tunable matching circuit for the tunable DVB-H antenna.

loss introduced by the two switches (over 0.7 dB each) and complicated layout. The structure with series of inductors shunted by control-FETs shown in Fig. 3.17b in this application has the short-coming of introducing a resonance near DVB-H band due to the open-state capacitance of the control-FET and the shunted inductor.

The structure of one varactor diode in series with an inductor Fig. 3.17a is chosen to approximate the tunable inductor, the inductance L_0 of the inductor and $C_{\max}$, $C_{\min}$ of the varactor diode should fulfill Equ. 3.13. As L_0 should be larger than 40 nH, it is chosen to be 48 nH to leave some tolerance margin. ω_1 and ω_2 are 470 and 702 MHz respectively. $C_{\max} = 14.3\,\text{pF}$ and $C_{\min} = 1.35\,\text{pF}$. An ASVP (anti-series varactor pair, MA4ST2300-CK by M/A-Com) with the total capacitance from around 1 to 17 pF is chosen. Fig. 5.3 shows the schematic of the tunable matching circuit. The top and the bottom layers of the printed circuit board are connected by vias for unique definition of the ground plane. The demonstrator is shown in Fig. 5.4.

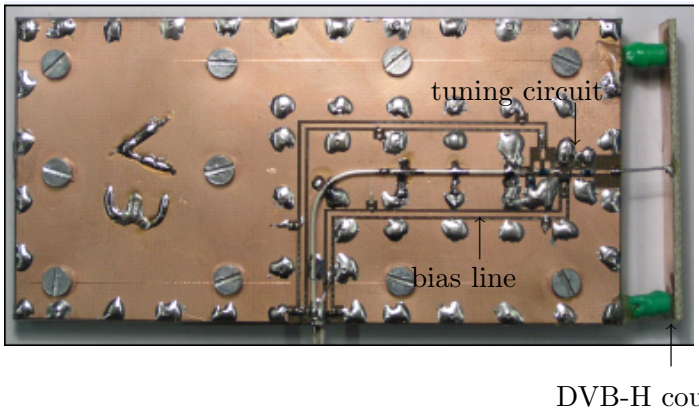

Figure 5.4: Photo of the DVB-H tunable antenna.

5.3.2 Measured impedance bandwidth

This attainable 7 dB band of the antenna is from 409 to 734 MHz for tuning voltages on the varactor diodes in the range from 0 to 5 V. The instantaneous bands at different tuning voltages are shown in Fig. 5.5 and listed in Tab. 5.1.

5.3.3 Antenna efficiency

The antenna efficiency is measured by Wheeler cap following the steps by [41] [42], and the efficiency in DVB-H band is above 27%, listed in Tab. 5.2.

5.4 Tunable DVB-H antenna together with EGSM 900 coupler

5.4.1 Antenna design

To avoid the exposure of the non-linear tuning devices to the EGSM TX signal, a two-port antenna structure is selected. The EGSM TX signal will first couple from the EGSM coupler to the printed circuit board, then couple to the DVB-H coupler from the printed circuit board [21]. These two coupling processes provide attenuation of the EGSM TX before it enters the tuning circuit. To maximize this effect while maintaining good coupling between each coupler and the printed circuit board, the DVB-H and the EGSM couplers are put at the opposite edges of the printed circuit board.

The matching circuit for the EGSM coupler is realized by two sections of microstrip lines on the printed circuit board. The schematic of the tunable matching circuit for DVB-H is shown in Fig. 5.6. Fig. 5.7 is the photo of the fabricated antenna.

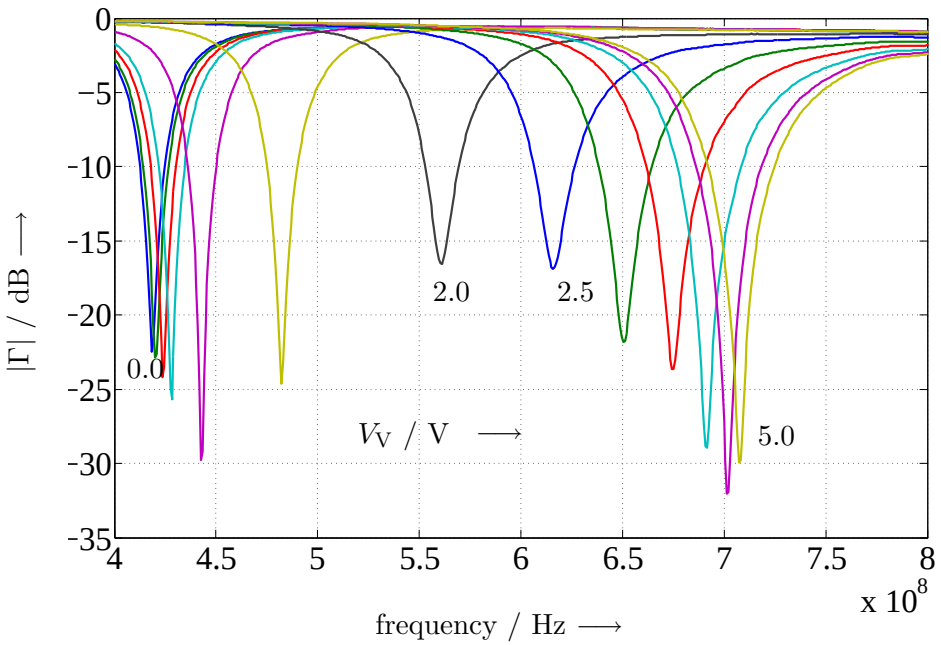

Figure 5.5: Measured reflection magnitude over frequency of the DVB-H tunable antenna for tuning voltages V_V in the range from 0 to 5 V.

Tuning voltage / V	7 dB band / MHz	bandwidth / MHz
0.0	409 - 427	18
0.1	411 - 430	19
0.3	415 - 434	19
0.5	419 - 438	19
1.0	432 - 453	21
1.5	471 - 494	23
2.0	548 - 574	26
2.5	601 - 633	32
3.0	632 - 672	40
3.5	654 - 700	46
4.0	670 - 716	46
4.5	679 - 728	49
5.0	685 - 734	51

Table 5.1: The obtained 7 dB instantaneous bands of the DVB-H tunable antenna for the tuning voltages in the range from 0 to 5 V.

V_V / V	frequency / MHz	efficiency / %
0.0	418.6	2.8
0.1	420.0	0.7
0.3	423.0	3.75
0.5	427.4	2.08
1.0	442.6	13.3
1.5	482.3	27.8
2.0	560.3	48.5
4.0	690.9	64.9
4.5	701.4	66.3
5.0	707.4	65.9

Table 5.2: The measured antenna efficiency of DVB-H antenna by Wheel cap.

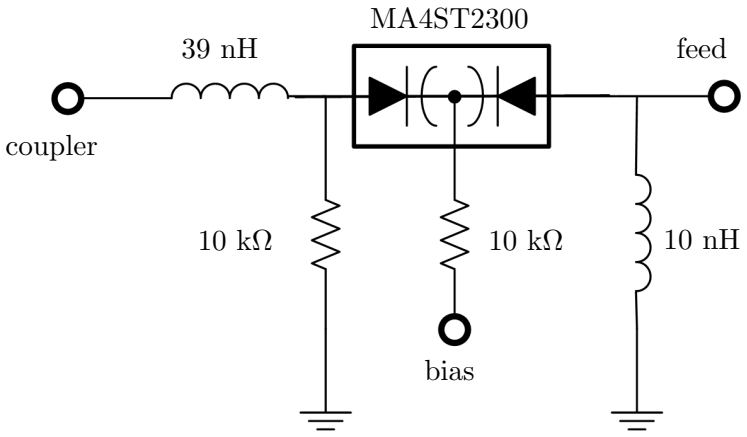

Figure 5.6: Schematic of the tunable matching circuit for the DVB-H antenna shown in Fig. 5.7. An EGSM coupler is fabricated on the same printed circuit board.

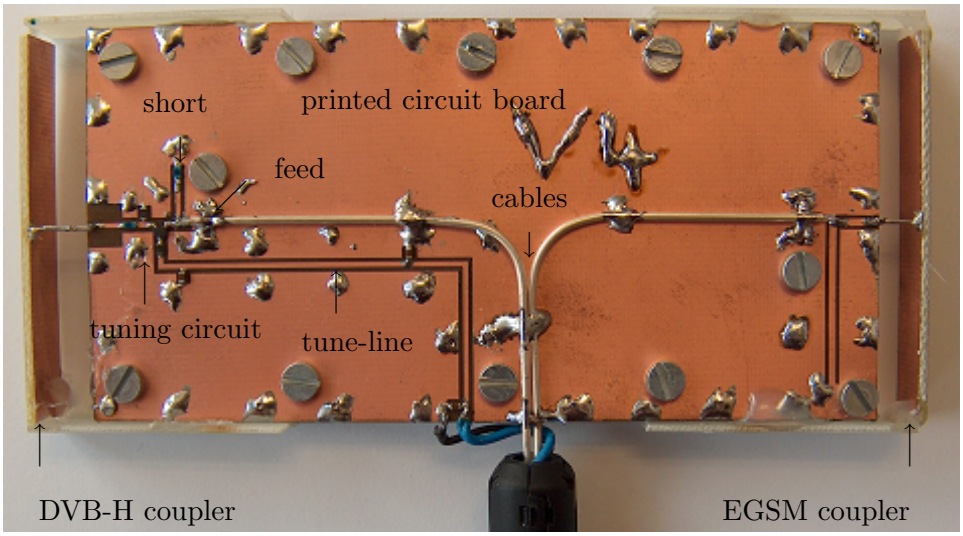

Figure 5.7: Photo of the tunable DVB-H antenna, together with an EGSM antenna attached to a 110 mm ×55 mm printed circuit board.

5.4.2 Measured impedance bandwidth

The measured band performance of DVB-H coupler at the tuning voltage from 0 to 5 V are listed in Tab. 5.3 and plotted in Fig. 5.8. The obtained 7 dB band is from 442 to 758 MHz.

The impact of DVB-H antenna tuning on the magnitude of the input reflection coefficient of the EGSM antenna is shown in Fig. 5.9. Graphs for 14 different values of the tuning voltages in the range from 0 V to 5 V are superimposed in the diagram. It can be observed that the dependency on the tuning voltage is little.

The isolation between the ports of the two antennas at different tuning voltages is shown in Fig. 5.10. The isolation in EGSM TX band is over 16 dB.

5.4.3 Non-linearity measurement results

Fig. 5.11 shows the result of the EGSM emission mask measurement. 33 dBm EGSM signal centered at 880 MHz was generated by signal generator, amplified by PA (power amplifier), and fed into the EGSM port of the tunable antenna. The spectrum of the radiated signal was measured by a receiving antenna. The (original) signal from PA was also measured after certain attenuation and normalization. Both of them are plotted in Fig. 5.11 together with emission mask defined in the standard [43] for comparison. And the distortion is slight.

Control Voltage / V	7 dB band / MHz
0.0	442 - 468
0.1	444 - 471
0.2	446 - 473
0.3	448 - 475
0.5	454 - 480
1.0	470 - 498
1.5	514 - 546
2.0	581 - 627
2.5	629 - 685
3.0	661 - 715
3.5	681 - 734
4.0	693 - 745
4.5	703 - 752
5.0	708 - 758

Table 5.3: The measured 7 dB bandwidth of the DVB-H tunable antenna with EGSM coupler for tuning voltages in the range from 0 to 5 V.

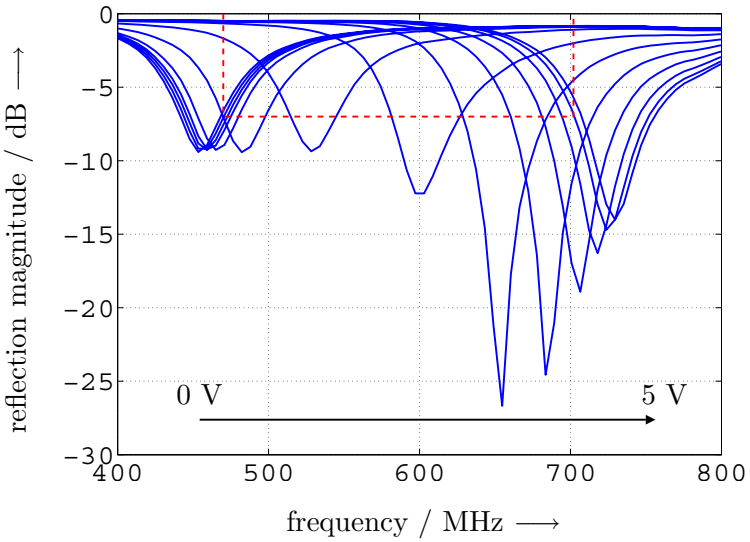

Figure 5.8: Measured reflection magnitude over frequency of the DVB-H coupler of the tunable antenna with EGSM exciter for tuning voltage in the range from 0 to 5 V. The dashed line denotes the target 7 dB return loss in the DVB-H band.

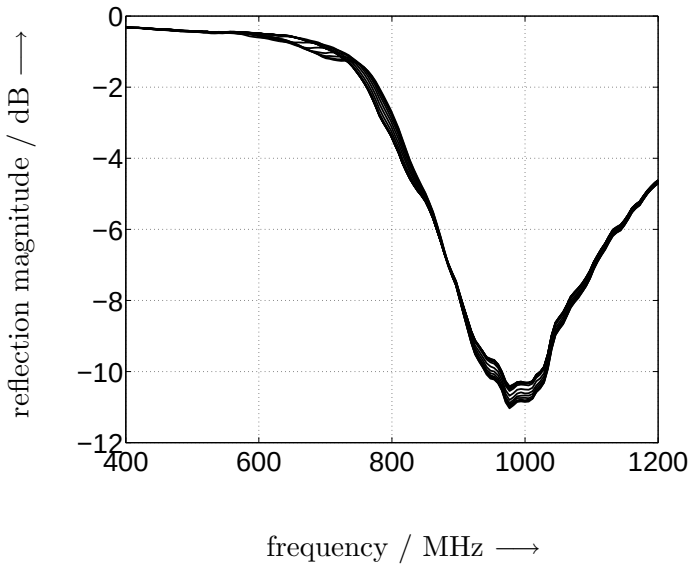

Figure 5.9: Measured reflection magnitude over frequency of the EGSM coupler of the tunable antenna with EGSM exciter for tuning voltages in the range from 0 to 5 V.

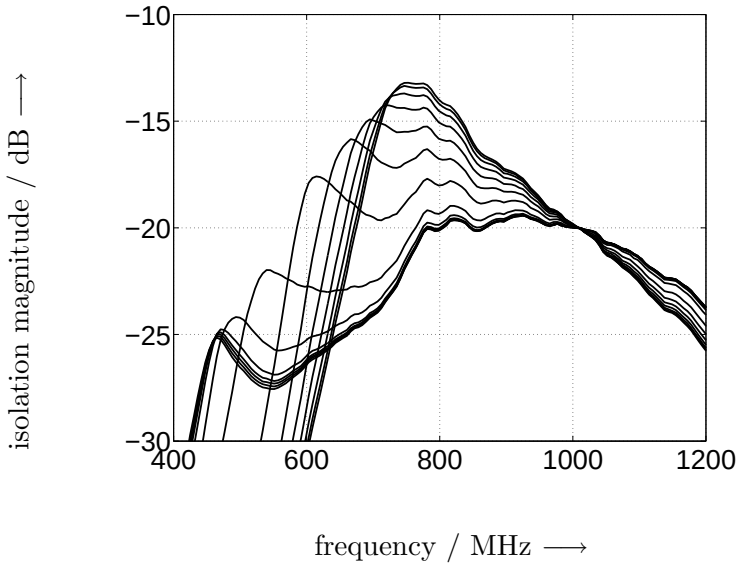

Figure 5.10: The measured isolation between the EGSM port and DVB-H port for tuning voltages in the range from 0 to 5 V.

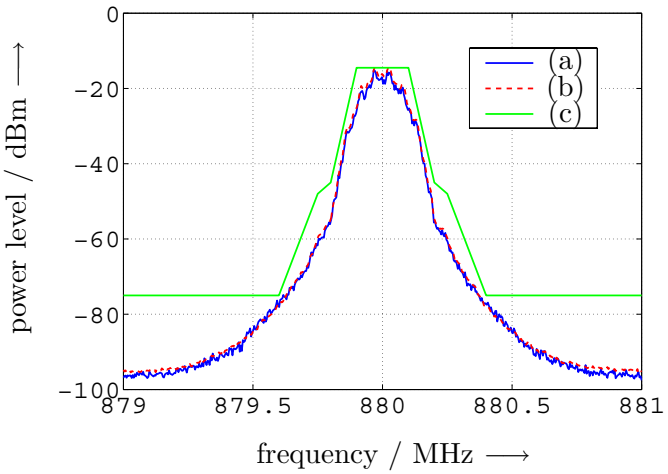

Figure 5.11: EGSM radiation distortion measurement in presence of tunable DVB-H antenna. (a) denotes the radiated signal by the EGSM coupler. (b) denotes the original signal from the power amplifier. (c) denotes the EGSM emission mask defined in standard.

The set-up for the blocker resilience measurement is shown in Fig. 5.12: a continuous-wave signal centered at 800 MHz is transmitted by a periodic logarithmic (peri-log) antenna, which imitates the UHF interferences in the environment, 33 dBm continuous wave signal centered at 900 MHz is fed into the EGSM port of the tunable DVB-H antenna to imitate the on-phone EGSM TX. The tuning voltage is set to 2.3 V. The mixing product at 700 MHz is measured at the DVB-H port after a BSF centered at 900 MHz. The measurement shows blocker resilience of 125 dB μV/m, which corresponds to over -8 dBm received power by a 100 mm dipole.

More stringent requirement is the spurious emission. 33 dBm continuous-wave signal was fed to the EGSM port. The harmonics generated by the

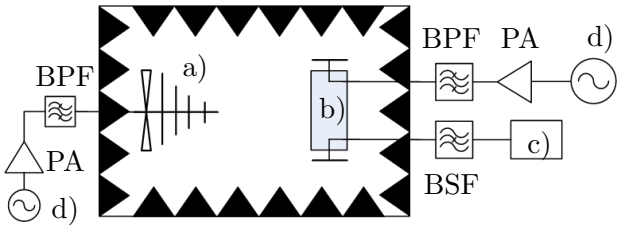

Figure 5.12: The experiment set-up for the blocker resilience measurement of the DVB-H tunable antenna, with a) peri-log antenna, b) terminal equipped with EGSM and tunable DVB-H antennas, c) spectrum analyzer, d) signal generator.

bias voltage / V	0.5	1.6	2.5	3.0	3.5
center frequency / MHz	470	550	650	680	710
2nd harmonic / dBm	−55.1	−36.4	−30.3	−29.1	−28.6
3rd harmonic / dBm	−53.7	−31.1	−33.2	−43.1	−35.1

Table 5.4: The harmonic radiation levels with different bias voltages, for the tunable DVB-H antenna together with EGSM antenna on a 110 mm ×55 mm printed circuit board.

antenna was measured by the receiving antenna, the total harmonics power was calculated based on the assumption that the antenna radiates the harmonics isotropically. Table 5.4 gives values of total harmonics power at different tuning voltages. At low tuning voltage (low operation band frequency), as higher isolation between the ports is achieved, lower harmonic radiation is observed. As the operation band tuned to higher frequency, 2nd harmonic level exceeds the standardized upper limit by less than 1.5 dB.

5.5 Harmonics suppression methods for DVB-H tunable antennas

As shown in Fig. 3.23, to isolate the anti-series varactor pair (ASVP) from the EGSM TX signal, passive modules can be added in the tunable matching circuit, which are

- module a) the module presenting "open" in EGSM TX band to block the TX,
- module b) the module presenting "short" in EGSM TX band to shunt TX current,
- module c) the module presenting "short" in EGSM TX band to divert the TX current to ground.

5.5.1 Modules presenting "short" in EGSM TX

The impedance between the two terminals of an L-C series circuit is 0 ("short") at its resonance frequency. Consider a series of an inductor L_1 and a capacitor C_1 which resonates at ω_{TX}, the center frequency of the GSM TX, the impedance of the series of L_1 and C_1 is

$$\begin{aligned} \mathrm{j}X =& \mathrm{j}\omega L_1 + \frac{1}{\mathrm{j}\omega C_1} \\ =& \mathrm{j}Z_1\Big(\frac{\omega}{\omega_{\mathrm{TX}}} - \frac{\omega_{\mathrm{TX}}}{\omega}\Big), \end{aligned} \tag{5.1}$$

L_1 (nH)	C_1 (pF)	C_P @ 702 MHz (pF)
10	3.15	8.1
20	1.57	4.1
50	0.63	1.6
100	0.32	0.81

Table 5.5: Selected combinations of L_1 C_1 to present "short" in EGSM 900 TX, and the maximum equivalent capacitance in DVB-H band of series L-C circuits.

with $Z_1 = \sqrt{\frac{L_1}{C_1}}$. The series of L_1 and C_1 presents a short at ω_TX, at the boundary of the TX band

$$\mathrm{j}X_\mathrm{boundary} = \pm\mathrm{j}Z_1 b_\mathrm{TX}, \tag{5.2}$$

with $b_\mathrm{TX} < 0.04$ the fractional bandwidth of GSM TX.

In DVB-H band, the L-C circuit shows capacitive whose equivalent capacitance C_P increases with the frequency. Selected combinations of L_1, C_1 and the equivalent parallel capacitances $C_\mathrm{P} = \frac{1}{\omega X}$ at $\omega = 2\pi \cdot 702$ MHz are listed in Tab. 5.5. Surface mounted inductors with inductance higher than 100 nH are not preferrable in mobile phone applications due to its large parasitic resistance. And surface mounted capacitors with capactance lower than 0.5 pF are few in the market.

5.5.2 Modules presenting "open" in EGSM TX

The impedance between the two terminals of a parallel of an L_2 and C_2 shown in Fig. 5.13 is infinite ("open") at its resonance frequency which is ω_TX. This circuit is inductive in DVB-H band, with the admittance of

$$\begin{aligned} \mathrm{j}B =& \mathrm{j}\omega C_2 + \frac{1}{\mathrm{j}\omega L_2} \\ =& \mathrm{j}Y\Big(\frac{\omega}{\omega_\mathrm{TX}} - \frac{\omega_\mathrm{TX}}{\omega}\Big), \end{aligned} \tag{5.3}$$

with $Y = \sqrt{\frac{C_2}{L_2}}$. The parallel L_2 and C_2 structure presents an "open" in EGSM TX and is inductive in DVB-H, with the equivalent inductance increasing with frequency. The equivalent inductances $L_\mathrm{S} = \frac{B}{\omega}$ at 702 MHz for different combinations of L_2 and C_2 are listed in Tab. 5.6.

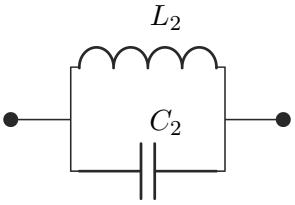

Figure 5.13: Structure of parallel L_2 and C_2 presenting "open" in EGSM TX band.

L_2 (nH)	C_2 (pF)	L_S @ 702 MHz (pF)
0.5	63.0	1.3
1	31.5	2.6
2	15.7	5.2
5	6.3	12.9
10	3.2	25.8
20	1.6	51.6
50	0.63	129

Table 5.6: Selected combinations of L_2 C_2 for the parallel L-C circuit shown in Fig. 5.13 which resonates at the center frequency of the EGSM 900 TX band, and the maximum equivalent inductance L_S in DVB-H band.

5.6 Tunable DVB-H antenna with EGSM 900 TX signal block

5.6.1 Tunable matching circuit

To isolate the varactors from the leak-in EGSM TX power, module a) shown in Fig. 3.23 is used to attenuate the EGSM TX before it reaches the varactors. To achieve high attenuation in the whole EGSM TX band, this module is implemented as a third-order Chebychev bandstop filter (BSF) with its stopband centered at EGSM TX. The schematic of the BSF is shown in Fig. 5.14. The simulated magnitude of transmission coefficient $|S_{21}|$ of this BSF considering the finite quality factors of the discrete devices is shown in Fig. 5.15. This BSF has over 48 dB attenuation in the EGSM 900 TX band.

The tunable matching circuit is shown in Fig. 5.16. The fabricated antenna is shown in Fig. 5.17.

5.6.2 Measured impedance bandwidth

Fig. 5.18 shows that the tunable DVB-H antenna covers the frequency range from 462 to 696 MHz (41% fractional bandwidth) with 7 dB return loss, for tuning voltages in the range from 0 V to 2.2 V. The dashed line denotes the

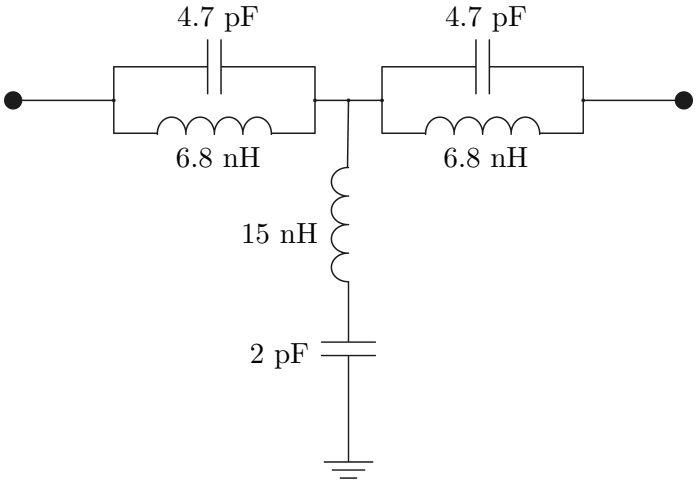

Figure 5.14: Schematic of the third-order bandstop filter used for EGSM TX blocking module for DVB-H tunable antenna.

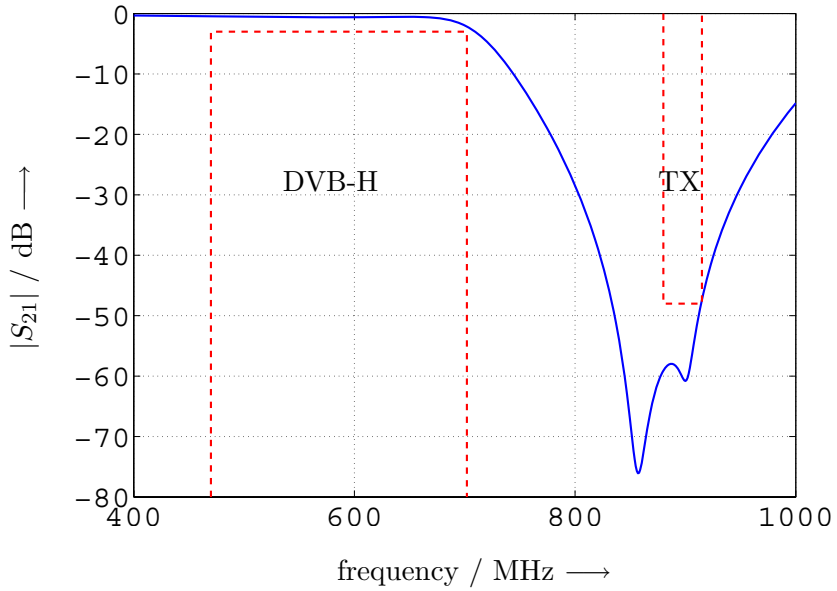

Figure 5.15: Simulated magnitude of the transmission coefficient of the 3rd-order BSF. The finite quality factors of the selected inductors and capacitors are taken into account. The dashed lines denote the DVB-H and EGSM TX bands.

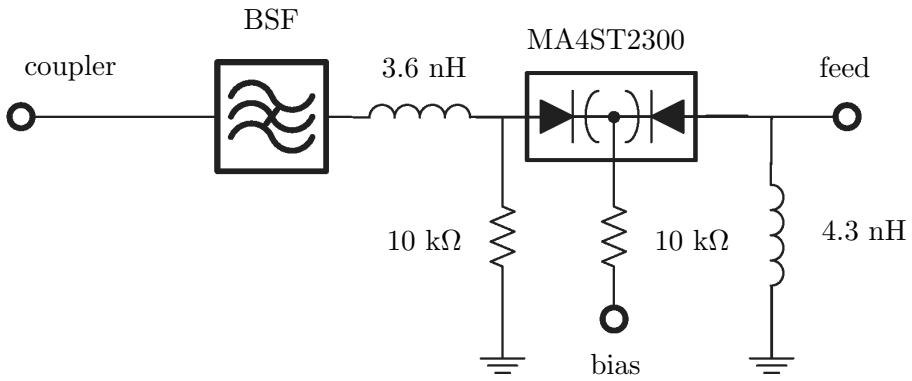

Figure 5.16: Schematic of the tunable matching circuit of tunable DVB-H antenna with a BSF to block the EGSM TX signal.

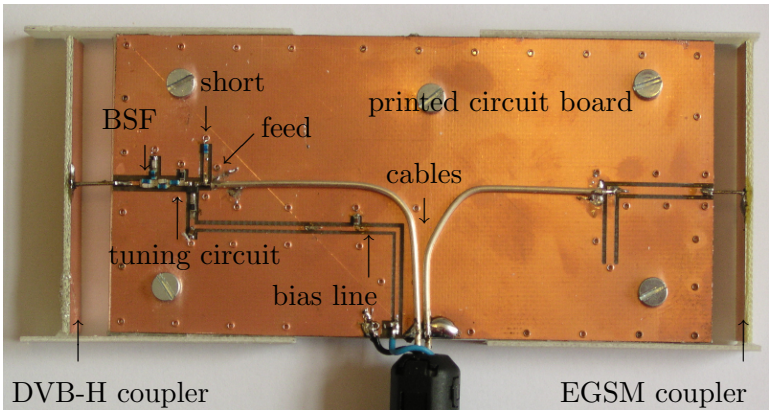

Figure 5.17: Photo of the tunable DVB-H antenna with EGSM TX block, together with an EGSM antenna attached to a 110 mm ×55 mm printed circuit board.

Control voltage / V	−7 dB band / MHz	Instantaneous bandwidth / MHz
0.0	462 - 492	30
0.1	466 - 495	31
0.3	473 - 502	29
0.5	481 - 511	30
0.8	496 - 525	29
1.0	510 - 539	29
1.2	530 - 558	28
1.5	574 - 604	30
1.8	625 - 657	32
2.0	656 - 682	28
2.2	683 - 696	13

Table 5.7: Measured 7 dB instantaneous band at different tuning voltages of the tunable DVB-H antenna with EGSM TX block

target 7 dB return loss in the DVB-H band. Tab. 5.7 lists the measured 7 dB instantaneous bandwidth at different tuning voltages. The instantaneous bandwidth is larger than 10 MHz. By redesign of the BPF it would be possible to increase the instantaneous bandwidth at 2.2 V tuning voltage and to cover the full DVB-H band.

The antenna covers the EGSM band with the return loss of 9 dB, shown in Fig 5.19. The change of the tuning voltage has little effect on the EGSM port.

The isolation between the two ports at different tuning voltages is shown in Fig. 5.20. The isolation in EGSM band is over 46 dB, which greatly alleviates the design of the BPF before the DVB-H receiver. This BPF can be designed with lower order which leads to lower insertion loss. Thus, the loss introduced by the tuning circuit including BSF and ASVP can be compensated by this BPF simplification.

5.6.3 Non-linearity measurement result

The in-band EGSM radiation spectrum is measured with 33 dBm EGSM signal centered at 880 MHz. The spectra of radiated signal and the (original) signal from the BPF after certain normalization are plotted in Fig. 5.21 together with emission mask defined in the standard [43] for comparison. And the distortion is slight.

The spurious emission measurement shows that the measured harmonics levels are over 16 dB below −30 dBm which is required by [43]. Table 5.8 gives values of maximum harmonics power at different tuning voltages.

For the blocker resilience measurement, as the isolation between the

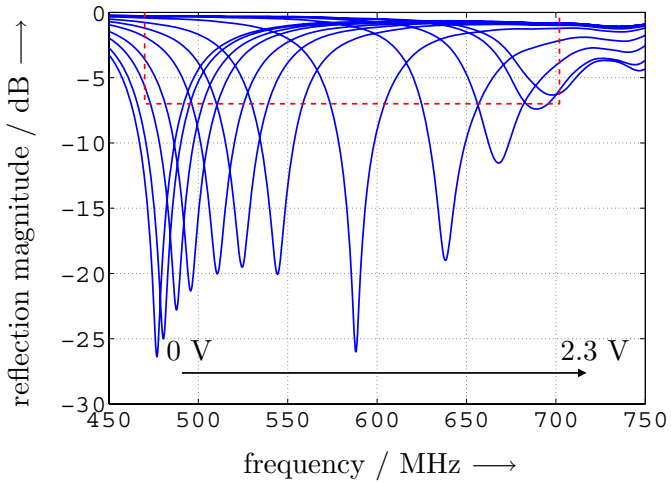

Figure 5.18: Measured reflection magnitude over frequency of the tunable DVB-H antenna with EGSM TX block at tuning voltage in the range from 0 to 2.3 V. The dashed line denotes the target 7-dB return loss in the DVB-H band.

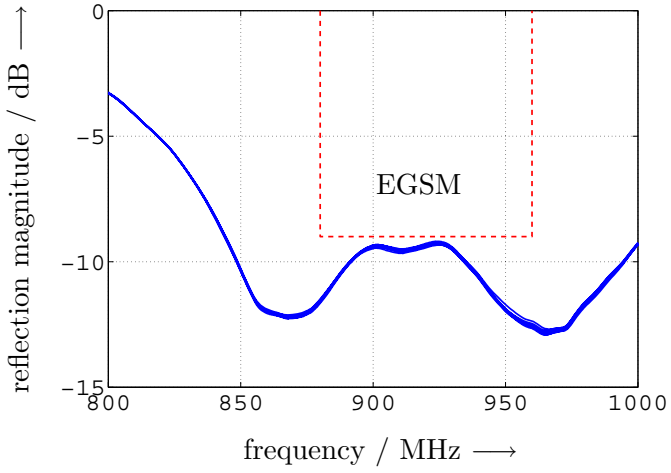

Figure 5.19: Measured reflection magnitude over frequency of the tunable DVB-H antenna with EGSM TX block for tuning voltage in the range from 0 to 2.3 V.

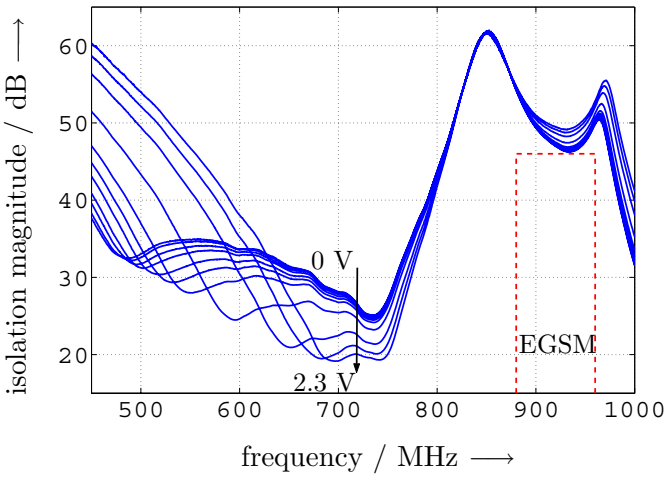

Figure 5.20: Measured isolation between the DVB-H and EGSM ports over frequency of the tunable DVB-H antenna with EGSM TX block for the tuning voltage in the range from 0 to 2.3 V.

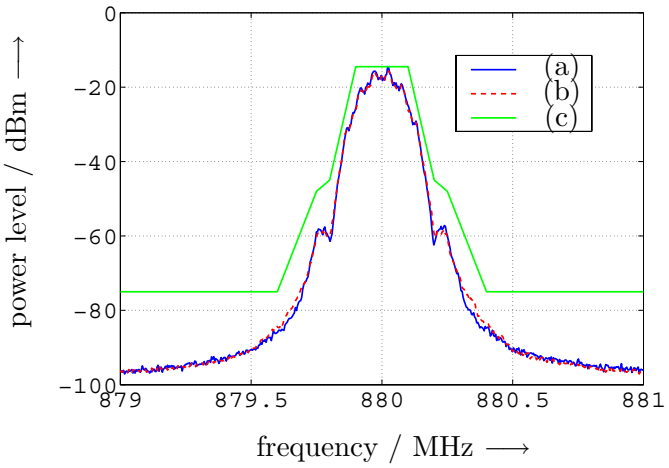

Figure 5.21: EGSM radiation distortion measurement in presence of the tunable DVB-H antenna with EGSM TX block. (a) denotes the radiated signal by the EGSM coupler. (b) denotes the original signal from the power amplifier. (c) denotes the EGSM emission mask defined in standard.

tuning voltage / V	0.0	0.5	1.0	1.5	2.0	2.3
2nd harmonic / dBm	−56.6	−56.6	−57.0	−56.5	−57.1	−57.0
3rd harmonic / dBm	−52.7	−51.8	−52.7	−52.8	−52.8	−53.0
4th harmonic / dbm	−48.2	−47.9	−47.4	−48.8	−47.7	−48.6
5th harmonic / dbm	−47.4	−47.1	−46.4	−46.8	−46.9	−47.6

Table 5.8: The harmonics radiation levels with different tuning voltages of the tunable DVB-H antenna with EGSM TX block.

Incident E / dB μV/m	125	130	135	140	142.5
EGSM TX 33 dBm at 900 MHz	NA	−122.5	−117.5	−107.5	−102.5
30 dBm	NA	NA	−120.5	−111.5	−105.5
27 dBm	NA	NA	NA	−112.5	−107.5
23 dbm	NA	NA	NA	−113.5	−109.5
20 dbm	NA	NA	NA	−114.5	−112.5

Table 5.9: The measured 3rd order intermodulation products at the DVB-H port of the 800 MHz incident electrical field at different field strength on the tunable DVB-H antenna with EGSM TX block and different levels of 900 MHz continuous-wave at the EGSM port.

DVB-H and EGSM 900 ports is over 60 dB, EGSM TX signal out of the DVB-H port is below −30 dBm. The notch filter between demonstrator and spectrum analyzer is omitted. The measured result at the tuning voltage of 2.3 V is listed in Tab. 5.9. The measurement shows excellent blocker resilience of over 140 dB μV/m, which corresponds to over 7 dBm received power by a 100 mm dipole.

Chapter 6

Conclusion

Nowadays mobile communication services require the mobile antenna to cover wider and wider band with satisfactory return loss. On the other hand, the size of the mobile terminal and the space available for the mobile antennas are shrinking. The attainable antenna bandwidth is subject to the physical limit depending on the size of the terminals. The shrinking available space and metal components like LCD and battery around make the coupling between the mobile antenna and the printed circuit board less efficient. As the result, it is hard to cover all the required band with good match. Tunable antenna is a solution.

Chapter 2 gives the physical limit on the attainable bandwidth of the mobile antennas. Tunable antenna is needed when the required bandwidth exceeds this physical limit. This chapter presents the existing solutions for the electrically small antennas to achieve wide band coverage.

Chapter 3 gives a systematic design procedure of the tunable antenna. The models of the antenna efficiency and the harmonics radiation are presented. The criteria to select the tuning devices are given also.

Chapter 4 points out the limitations of the standardized antenna measurement methods on the tunable antennas. New measurement set-ups and procedures are proposed to measure the in-band radiation spectrum, out-of-band spurious emission and the blocker resilience of the tunable antennas. The linearity of the tunable antennas can be characterized by these measurement methods.

Following the design procedure, in Chapter 5, a DVB-H tunable antenna is designed and fabricated on a 110 mm $\times$55 mm printed circuit board as a demonstrator. It is estimated in Chapter 2 that any non-tunable antenna constructed on this printed circuit board can not cover DVB-H band with more than 7 dB return loss. A bandstop filter is used to suppress the isolate the tuning elements from the EGSM TX signal. This antenna covers the DVB-H band with better than 7 dB return loss. Despite the highly non-linear varactor diodes used in the design, this antenna is highly linear.

Chapter 7

Appendix

7.1 GSM application requirements

GSM 850, GSM 900, GSM 900 (including P-GSM and EGSM), DCS 1800 and PCS 1900 are the GSM bands used for today's mobile applications. GSM 900 and DCS 1800 are used in Europe and most Asian countries including China. GSM 850 and PCS 1900 are used in USA and Latin America.

Specifications of GSM are given in [31] [43]. This section summarizes the parts related to the mobile frontend.

Frequency band

The frequency bands for GSM 850, GSM 900, DCS 1800 and PCS 1900 are listed in Tab. 7.1.

Mobile station (MS) output power

The requirement of the output power is given in terms of power levels at the antenna connector of the equipment. The maximum output power of the mobile station, according to its class, are defined in Tab. 7.2 7.3.

In practice, the maximum power level in mobile phone is 33 dBm. This value is used throughout this thesis.

	mobile transmit (TX)	base transmit (RX)
GSM 850	824 - 849 MHz	869 - 894 MHz
P-GSM 900	890 - 915 MHz	935 - 960 MHz
EGSM 900	880 - 915 MHz	925 - 960 MHz
DCS 1800	1710 - 1785 MHz	1805 - 1880 MHz
PCS 1900	1850 -1910 MHz	1930 - 1990 MHz

Table 7.1: The frequency bands of GSM in mobile applications [43].

Power class	GSM850 GSM900	DCS1800	PCS1900
1		1 W(30 dBm)	1 W(30 dBm)
2	8 W(39 dBm)	0.25 W(24 dBm)	0.25 W(24 dBm)
3	5 W(37 dBm)	4 W(36 dBm)	2 W(33 dBm)
4	2 W(33 dBm)		
5	0.8 W(29 dBm)		

Table 7.2: The GSM power levels of the mobile station for GMSK modulation for different power classes specified in [43].

Power class	GSM850 GSM900	DCS1800	PCS1900
E1	33 dBm	30 dBm	30 dBm
E2	27 dBm	26 dBm	26 dBm
E3	23 dBm	22 dBm	22 dBm

Table 7.3: The GSM power levels of the mobile station for 8-PSK modulation for different power classes specified in [43].

Output RF spectrum

The inband RF spectrum of GSM is specified in Tab. 7.4 7.5 7.6, in frequency-hopping mode as well as in non-frequency-hopping mode. The measurement conditions are given in section 4.2.1 in [43].

The mask representations of these specifications are shown in Fig. 7.1, 7.2, 7.3 and 7.4.

The exceptions listed in Tab. 7.7 shall apply if a requirement in Tab. 7.4 7.5 7.6 is tighter than the limit given in Tab. 7.7.

Spurious emissions

Measuring conditions

GSM 850 and GSM 900 MS								
	100	200	250	400	≥ 600 < 1800	≥ 1800 < 3000	≥ 3000 < 6000	≥ 6000
≥ 39	+0.5	−30	−33	−60	−66	−69	−71	−77
37	+0.5	−30	−33	−60	−64	−67	−69	−75
35	+0.5	−30	−33	−60	−62	−65	−67	−73
≤ 33	+0.5	−30	−33	−60*	−60	−63	−65	−71
NOTE: * For equipment supporting 8-PSK, the requirement is −54 dB								

Table 7.4: The maximum allowed mobile station inband output RF power level (in dBm) at different frequency offset (in kHz) from the carrier for different peak power (in dBm), for GSM 850 and 900. [43]

DCS1800 MS							
	100	200	250	400	≥ 600 < 1800	≥ 1800 < 6000	≥ 6000
≥ 36	+0.5	−30	−33	−60	−60	−71	−79
34	+0.5	−30	−33	−60	−60	−69	−77
32	+0.5	−30	−33	−60	−60	−67	−75
30	+0.5	−30	−33	−60*	−60	−65	−73
28	+0.5	−30	−33	−60*	−60	−63	−71
26	+0.5	−30	−33	−60*	−60	−61	−69
≤ 24	+0.5	−30	−33	−60*	−60	−59	−67
NOTE: * For equipment supporting 8-PSK, the requirement is −54 dB							

Table 7.5: The maximum allowed mobile station inband output RF power level (in dBm) at different frequency offset (in kHz) from the carrier for different peak power (in dBm), for DCS 1800. [43]

PCS1900 MS								
	100	200	250	400	≥ 600 < 1200	≥ 1200 < 1800	≥ 1800 < 6000	≥ 6000
≥ 33	+0.5	−30	−33	−60	−60	−60	−68	−76
32	+0.5	−30	−33	−60	−60	−60	−67	−75
30	+0.5	−30	−33	−60*	−60	−60	−65	−73
28	+0.5	−30	−33	−60*	−60	−60	−63	−71
26	+0.5	−30	−33	−60*	−60	−60	−61	−69
≤ 24	+0.5	−30	−33	−60*	−60	−60	−59	−67
NOTE: * For equipment supporting 8-PSK, the requirement is −54 dB								

Table 7.6: The maximum allowed mobile station inband output RF power level (in dBm) at different frequency offset (in kHz) from the carrier for different peak power (in dBm), for PCS 1900. [43]

Frequency offset from the carrier	GSM 900 GSM 850	DCS 1800 PCS 1900
<600 kHz	−36 dBm	−36 dBm
≥600 kHz, <1800 kHz	−51 dBm	−56 dBm
≥1800 kHz	−46 dBm	−51 dBm

Table 7.7: The exceptions of the inband power level at different frequency offset from the carrier for GSM. [43]

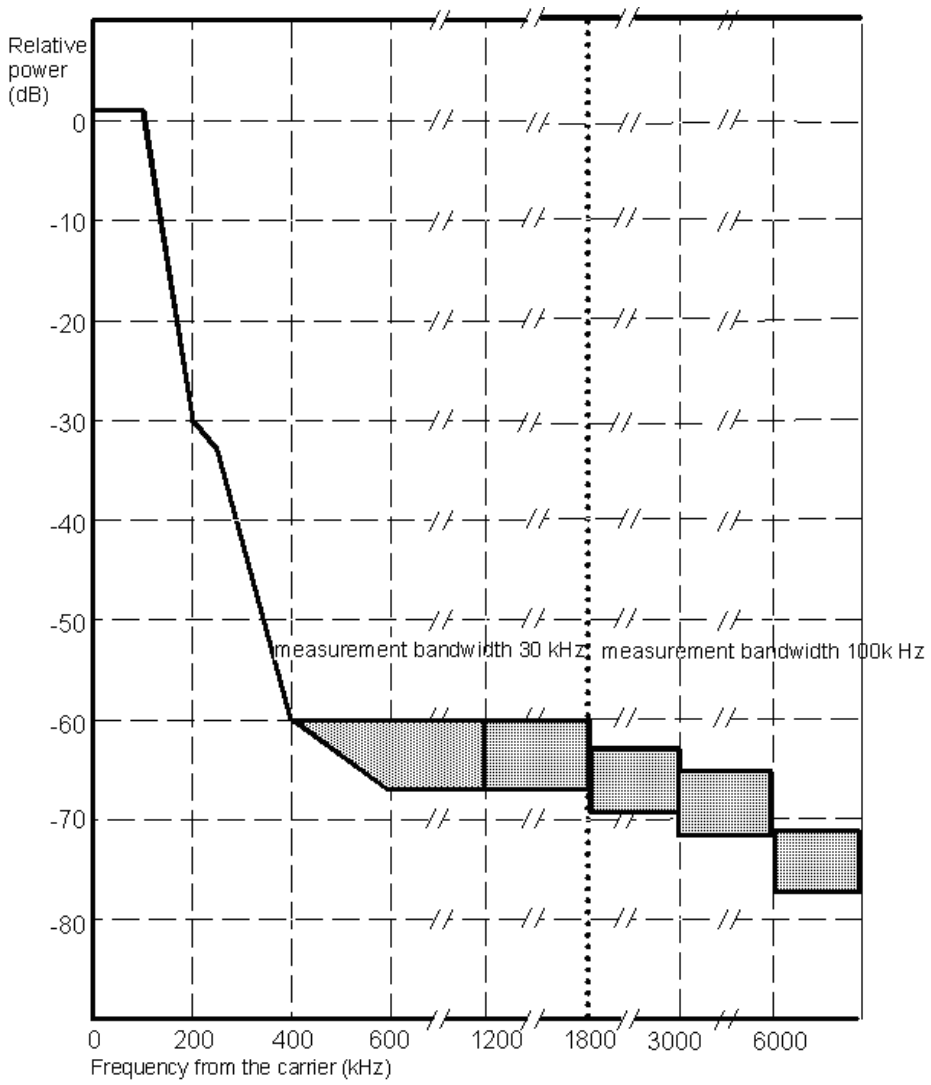

Figure 7.1: GSM 400, GSM 900, GSM 850 and GSM 700 mobile station spectrum due to GMSK modulation, from [43].

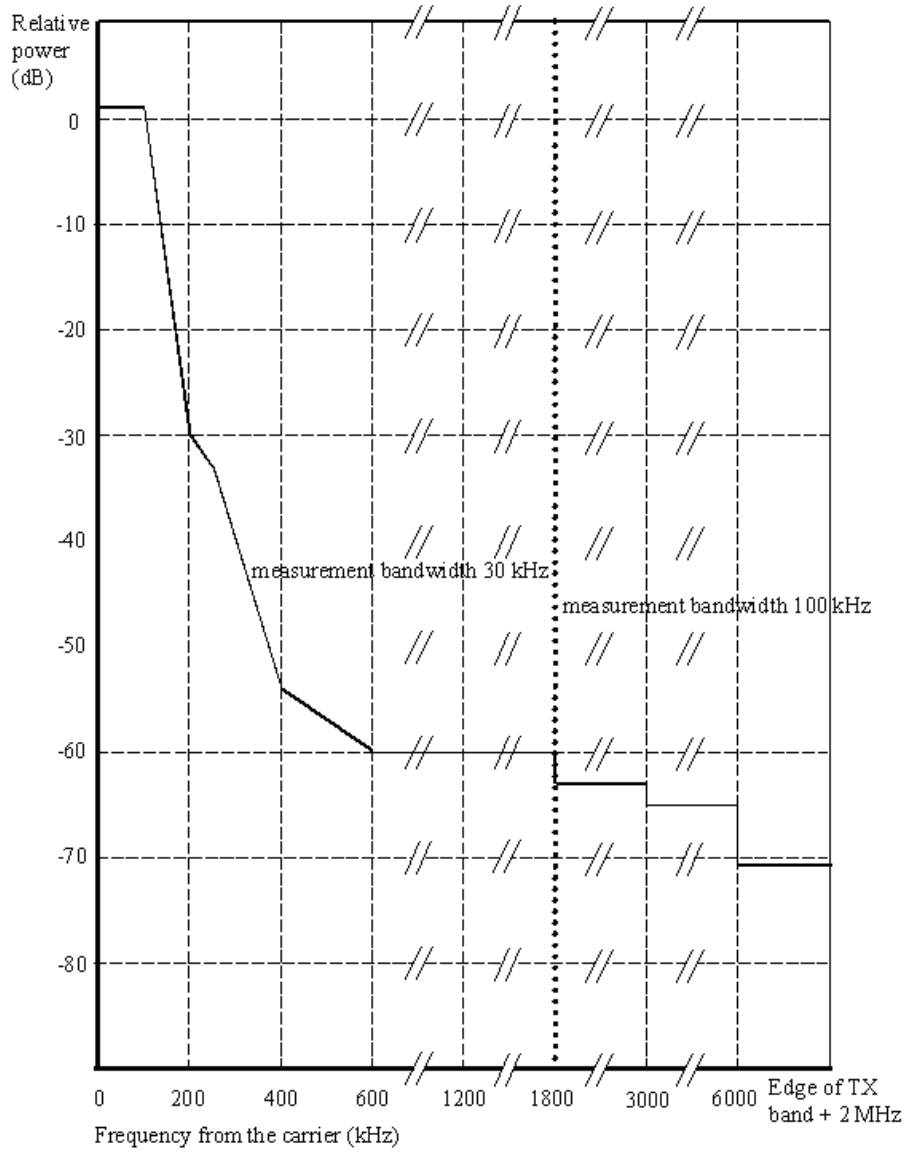

Figure 7.2: GSM 400, GSM 900, GSM 850 and GSM 700 mobile station spectrum due to 8PSK modulation, from [43].

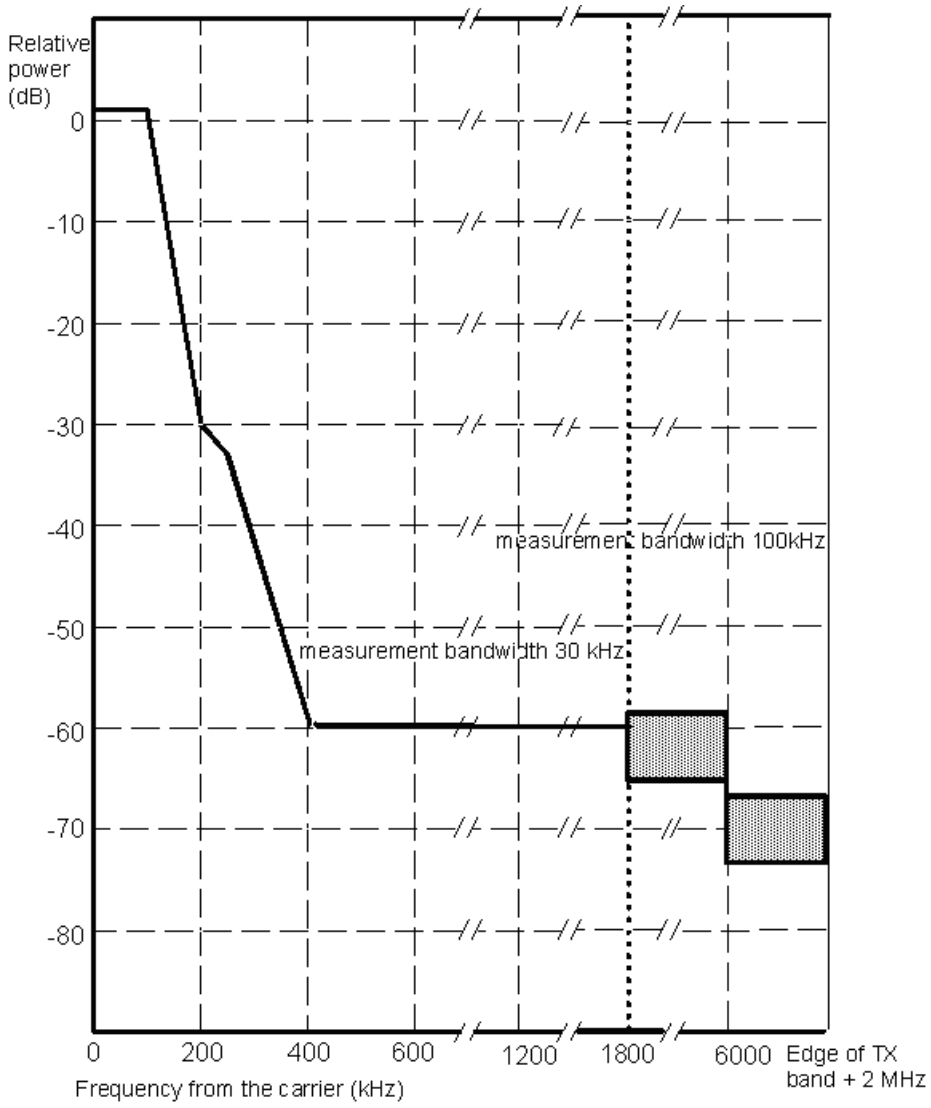

Figure 7.3: DCS 1800 and PCS 1900 mobile station spectrum due to GMSK modulation, from [43].

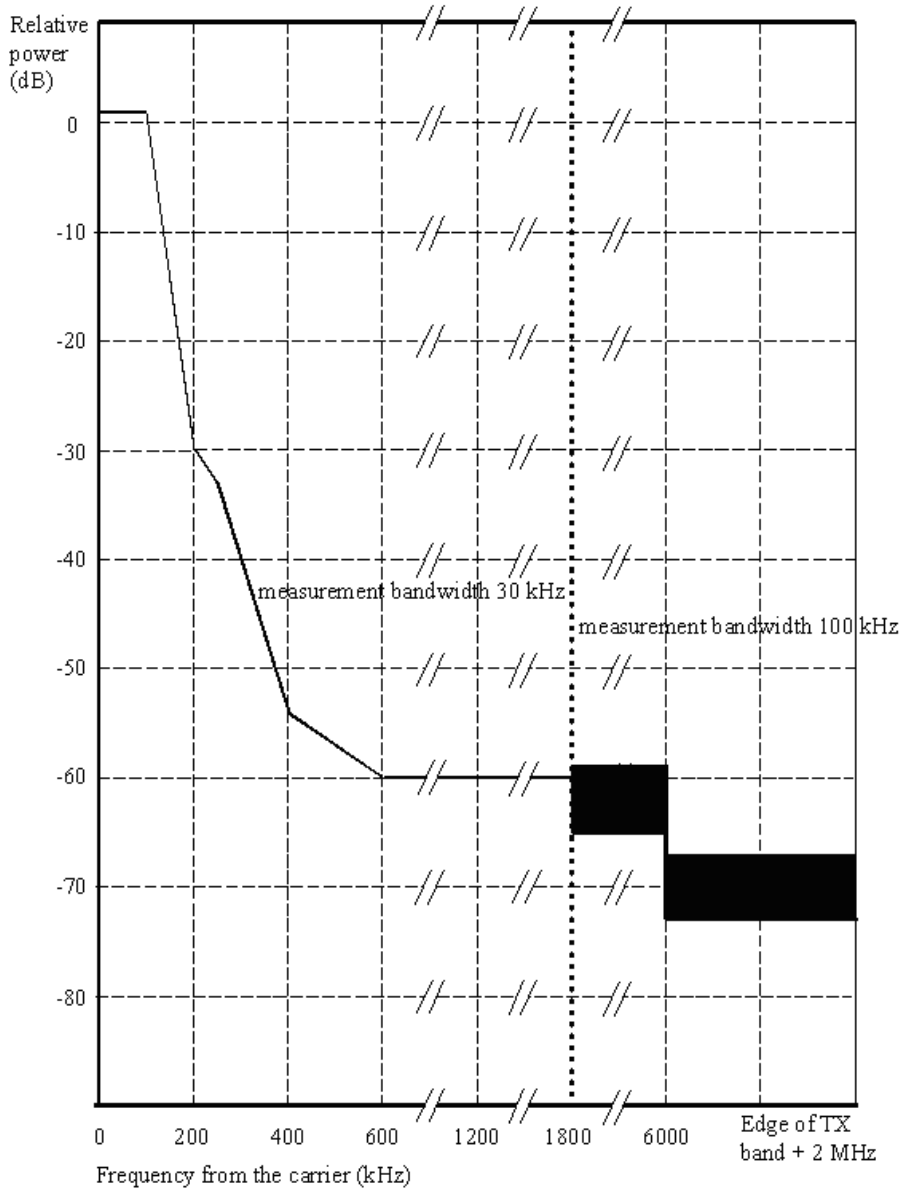

Figure 7.4: DCS 1800 and PCS 1900 mobile station spectrum due to 8PSK modulation, from [43].

The spurious emissions are specified by measuring the peak power in a given bandwidth at various frequencies. The measurement bandwidth is increased as the frequency offset between the measurement frequency and either the carrier or the edge of the MS transmit band, increases. The measurement bandwidth is classified into two categories [43]:

category a:

Frequency offset from carrier	Measurement bandwidth
$\geq$ 1.8 MHz	30 kHz
$\geq$ 6 MHz	100 kHz

category b:

Band	Frequency offset	Measurement bandwidth
100 kHz to 50 MHz		10 kHz
50 MHz to 500 MHz outside the relevant transmit band	(offset from edge of the relevant transmit band)	
	$\geq$ 2 MHz	30 kHz
	$\geq$ 5 MHz	100 kHz
above 500 MHz outside the relevant transmit band	(offset from edge of the relevant transmit band)	
	$\geq$ 2 MHz	30 kHz
	$\geq$ 5 MHz	100 kHz
	$\geq$ 10 MHz	300 kHz
	$\geq$ 20 MHz	1 MHz
	$\geq$ 30 MHz	3 MHz

GSM900 and DCS1800

The power measured in the conditions specified in category a for a MS when allocated a channel, shall be no more than −36 dBm [43].

The power measured in the conditions specified in category b for a MS, when allocated a channel, shall be no more than [43]:

250 nW (−36 dBm) in the frequency band 9 kHz to 1 GHz;

1 μW (−30 dBm) in the frequency band 1 GHz to 12,75 GHz.

The power measured in a 100 kHz bandwidth for a MS, when not allocated a channel (idle mode), shall be no more than (see also note in subclause 4.3.1 above):

2 nW (−57 dBm) in the frequency bands 9 kHz to 1 000 MHz;

20 nW (−47 dBm) in the frequency bands 1 12.75 GHz,

with the following exceptions:

1.25 nW (−59 dBm) in the frequency band 880 MHz to 915 MHz;

1.25 nW (−59 dBm) in the frequency band 870 MHz to 915 MHz for T-GSM 900;

5 nW (−53 dBm) in the frequency band 1.71 GHz to 1.785 GHz;

−76 dBm in the frequency bands 1900 ∼ 1920 MHz, 1920 ∼ 1980 MHz, 2010 ∼ 2025 MHz, and 2210 ∼ 2170 MHz.

GSM850 and PCS 1900

The peak power measured in the conditions specified in category a, for a MS when allocated a channel, shall be no more than −36 dBm [43].

The peak power measured in the conditions specified in category b, for a MS, when allocated a channel, shall be no more than [43]:

−36 dBm in the frequency band 9 kHz to 1 GHz;

−30 dBm in all other frequency bands 1 GHz to 12,75 GHz.

The peak power measured in a 100 kHz bandwidth for a mobile, when not allocated a channel (idle mode), shall be no more than:

−57 dBm in the frequency bands 9 kHz to 1000 MHz;

−53 dBm in the frequency band 1850 MHz to 1910 MHz;

−47 dBm in all other frequency bands 1 GHz to 12,75 GHz.

The power emitted by the MS in a 100 kHz bandwidth using the measurement techniques for modulation and wide band noise (subclause 4.2.1) shall not exceed:

−79 dBm in the frequency band 698 MHz to 710 MHz

−73 dBm in the frequency band 710 MHz to 716 MHz

−79 dBm in the frequency band 747 MHz to 757 MHz

−73 dBm in the frequency band 757 MHz to 762 MHz

−79 dBm in the frequency band 869 MHz to 894 MHz;

−71 dBm in the frequency band 1930 MHz to 1990 MHz.

A maximum of five exceptions with a level up to −36 dBm are permitted in each of the band 698 MHz to 716 MHz, 747 MHz to 762 MHz, 869 MHz to 894 MHz and 1930 MHz to 1990 MHz for each ARFCN used in the measurements.

7.2 Mobile and portable DVB-T application requirements

The specifications of the radio access interface of the mobile and portable DVB-T are given in [17]. Those relative to the RF frontend are listed below.

Terminal categories

Three categories of the terminals are specified in [17]:

1. Integrated car terminals: DVB-T terminals is installed in a car and the antenna is integral with the car.

2. Portable digital TV sets: Terminals are intended for receiving normal MPEG-2 based digital TV services indoors and outdoors with attached antennas. This category is divided to two sub-categories:

   (a) The receiver screen size is typically greater than 25 cm and the receiver may be battery or AC powered. Typically the terminal is stationary during the reception. An example of the antenna may be an adjustable telescope or wide-band design, either active or passive , attached to the receiver.

   (b) Pocketable digital TV-receiver. The terminal is battery operated and can be moved during use. Usually the antenna is integral with the terminal.

3. Hand-held portable convergence terminals: This category covers small battery powered hand-held convergence terminals with build-in cellular radio like GSM, GPRS or UMTS. The terminals have the functionality of a mobile phone and can receive IP-based services over DVB-T. The DVB-T antenna and the cellular antenna are both integral with the terminal.

Frequencies and channel bandwidths

Channel frequencies

The channel frequencies of band III, IV and V are given below. 6, 7 and 8 MHz channel rasters are used in various countries. The centre frequencies f_c of the incoming DVB-T RF signals are:

VHF III

- For countries using 8 MHz channel raster
  $f_c = 178\ \text{MHz} + (N-6) \times 8\ \text{MHz} + f_{\text{offset}}$, with $N = \{6, \cdots, 12\}$ (VHF channel number).

- For countries using 7 MHz channel raster
  $f_c = 177.5\ \text{MHz} + (N-5) \times 7\ \text{MHz} + f_{\text{offset}}$, with $N = \{5, \cdots, 12\}$ (VHF channel number).

- For countries using 6 MHz channel raster
  $f_c = 177.0\ \text{MHz} + (N-7) \times 6\ \text{MHz} + f_{\text{offset}}$, with $N = \{7, \cdots, 13\}$ (VHF channel number).

In some countries offsets may be used, preferred offset is $\pm n \times 1/6$ MHz, with $n = \{1, 2, \cdots\}$.

UHF IV and V

- For countries using 8 MHz channel raster
  $f_c = 474\ \text{MHz} + (N-21) \times 8\ \text{MHz} + f_{\text{offset}}$, with $N = \{21, \cdots, 69\}$ (UHF channel number). The total band ranges from 470 MHz to 862 MHz.

- For countries using 7 MHz channel raster
  $f_c = 529.5$ MHz $+ (N - 28) \times 7$ MHz $+ f_{\text{offset}}$, with $N = \{28, \cdots, 67\}$ (UHF channel number). The total band ranges from 526 MHz to 806 MHz.

- For countries using 6 MHz channel raster
  $f_c = 473$ MHz$+(N-14)\times 6$ MHz$+f_{\text{offset}}$, with $N = \{14, \cdots, 83\}$ (UHF channel number). The total band ranges from 470 MHz to 890 MHz.

In some countries frequency offsets f_{offset} may be used, preferred offset is $\pm n \times 1/6$ MHz, with $n = \{1, 2, \cdots\}$. In UK $n = 1$.

Supported frequency ranges

The receivers in Terminal Categories 1 and 2a shall be able to receive all the channels in the VHF band III and UHF bands IV and V. The receivers in Terminal Category 2b shall be able to receive all channels in UHF bands IV and V, VHF III is an option depending on the market area needs. The receivers in Terminal Category 3 shall be able to receive all channels in UHF band IV and V, if the terminal does not support GSM 900.

In case GSM 900 is used in a convergence terminal (category 3), the usable frequency range is limited to channel 49 [698 MHz] due to the interoperability considerations.

Terminal category	VHF III	UHF IV	UHF V
1 Integrated car terminals	Yes	Yes	Yes
2a Portable digital TV-Sets	Yes	Yes	Yes
2b Pocketable TV-Sets	Optional	Yes	Yes
3 Convergence terminals	No	Yes	Yes or up to ch. 49 See text above

Supported bandwidths

The receiver should support the 6,7 and 8 MHz bandwidths according to the market area needs.

Minimum and maximum receiver signal input levels

Noise floor

The receiver shall have a noise figure better than 5 dB at the reference point at sensitivity level of each DVB-T mode. The noise floor power levels corresponding to different channel bandwidths are:

- $P_n = -100.2$ dBm, for 8 MHz channels, BW=7.61 MHz,
- $P_n = -100.7$ dBm, for 7 MHz channels, BW=6.66 MHz,
- $P_n = -101.4$ dBm, for 6 MHz channels, BW=5.71 MHz.

Minimum input levels for the receiver

Detailed statement on minimum input levels for different DVB-T mode and channel conditions is given in [17].

Total maximum power for wanted and unwanted signals

- For terminal category 1: The maximum total power from the wanted and unwanted signals shall be less than -15 dBm.
- For terminal category 2: The maximum total power from the wanted and unwanted signals shall be less than -25 dBm.

7.3 Basics of the TLM method

The transmission-line matrix (TLM) method is a space and time discretizing method of electromagnetic field computation. It was introduced by Johns [44]. The TLM method can be used to model complex electromagnetic structures. Detail descriptions are given in [45] [46] [47] [48] [49] [50].

TLM method solves the Maxwell equations

$$\nabla \times \vec{H} = \vec{j} + \frac{\partial \vec{D}}{\partial t} \tag{7.1}$$

$$\nabla \times \vec{E} = -\frac{\partial \vec{B}}{\partial t} \tag{7.2}$$

$$\nabla \cdot \vec{D} = \rho \tag{7.3}$$

$$\nabla \cdot \vec{B} = 0 \tag{7.4}$$

by mapping the electric and magnetic field in space to the voltage and current in the transmission-line network. I summarize the basics of TLM method following [51].

The space is discretized in cells. On every surface of the cell samples of tangential electric and magnetic fields are taken. There are 12 electric field samples and 12 magnetic samples per cell. The sampled field components at $(x = l\Delta l, y = m\Delta l, z = n\Delta l, t = k\Delta t)$ are summarized in 12-dimensional vectors

$$ {}_k\mathbf{E}_{l,m,n} = {}_k[E_1, E_2, E_3, E_4, E_5, E_6, E_7, E_8, E_9, E_{10}, E_{11}, E_{12}]^T_{l,m,n}, \tag{7.5}$$

$$ {}_k\mathbf{H}_{l,m,n} = {}_k[H_1, H_2, H_3, H_4, H_5, H_6, H_7, H_8, H_9, H_{10}, H_{11}, H_{12}]^T_{l,m,n}. \tag{7.6}$$

Fig. 7.5 shows the symmetrical condensed node (SCN) or TLM cell. It consists of 12 ports to represent 2 polarizations in each coordinate direction. The scattering matrix of this 12-port network is [51]

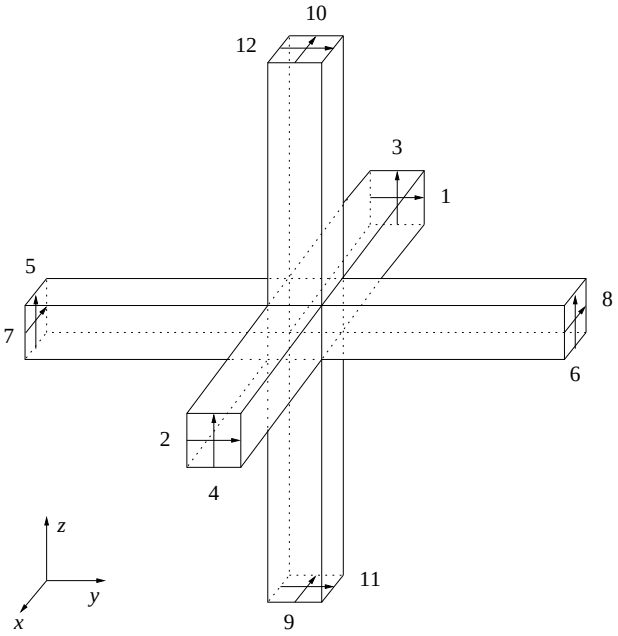

Figure 7.5: The condensed symmetric TLM node [51].

$$\mathbf{S} = \begin{bmatrix} 0 & \mathbf{S}_0 & \mathbf{S}_0^T \\ \mathbf{S}_0^T & 0 & \mathbf{S}_0 \\ \mathbf{S}_0 & \mathbf{S}_0^T & 0 \end{bmatrix} \text{ with } \mathbf{S}_0 = \frac{1}{2}\begin{bmatrix} 0 & 0 & 1 & -1 \\ 0 & 0 & -1 & 1 \\ 1 & 1 & 0 & 0 \\ 1 & 1 & 0 & 0 \end{bmatrix}. \tag{7.7}$$

The wave amplitude vectors

$$ {}_k\mathbf{a}_{l,m,n} = {}_k[a_1, a_2, a_3, a_4, a_5, a_6, a_7, a_8, a_9, a_{10}, a_{11}, a_{12}]^T_{l,m,n}, \tag{7.8}$$

$$ {}_k\mathbf{b}_{l,m,n} = {}_k[b_1, b_2, b_3, b_4, b_5, b_6, b_7, b_8, b_9, b_{10}, b_{11}, b_{12}]^T_{l,m,n} \tag{7.9}$$

gives the incident and scattered waves normal to the surfaces of the TLM cell. The wave amplitudes and the field components are related via

$$ {}_k\mathbf{E}_{l,m,n} = \sqrt{Z_F}({}_k\mathbf{a}_{l,m,n} +_k \mathbf{b}_{l,m,n}), \tag{7.10}$$

$$ {}_k\mathbf{H}_{l,m,n} = \frac{1}{\sqrt{Z_F}}({}_k\mathbf{a}_{l,m,n} -_k \mathbf{b}_{l,m,n}), \tag{7.11}$$

with $Z_F = \sqrt{\frac{\mu}{\epsilon}}$ the field impedance.

Bibliography

[1] L. J. Chu, "Physical limitations of omni-directional antennas," *J. Appl. Phys.*, vol. 19, pp. 1163–1175, Dec. 1948.

[2] J. S. McLean, "A re-examination of the fundamental limits on the radiation q of electrically small antennas," *IEEE Trans. Antennas Propagat.*, vol. 44, no. 5, pp. 672–676, May 1996.

[3] L. Huang, W. L. Schroeder, and P. Russer, "Estimation of maximum attainable antenna bandwidth in electrically small mobile terminals," in *36th European Microwave Conf. Proc.*, Manchester, UK, Sep. 2006.

[4] D. Auckland, S. Rogers, and J. Aberle, "Reconfigurable antennas and RF front ends for portable wireless devices," in *Proc.2002 Software Defined Radio Technical Conference*, 2002, pp. 29–33.

[5] D. T. Auckland and S. D. Rogers, "Reconfigurable antennas and RF front-ends for portable wireless devices," 2002, presentation by Etenna Corporation.

[6] J. T. Aberle, S.-H.-Ohn, D. T. Auckland, and S. D. Rogers, "Reconfigurable antennas for portable wireless devices," *IEEE Antennas Propagat. Mag.*, vol. 45, no. 6, pp. 148–154, Dec. 2003.

[7] O. Kivekäs, J. Ollikainen, and P. Vainikainen, "Frequency-tunable internal antenna for mobile phones," in *COST 284 JINA contribution*, Nice, France, Nov. 2002, (http://www.cost284.com).

[8] N. C. Karmakar, "Shorting strap tunable single feed dual-band stacked patch PIFA," *IEEE Antennas Wireless Propagat. Lett.*, vol. 2, no. 2, pp. 68–71, 2003.

[9] ——, "Shorting strap tunable stacked patch PIFA," *IEEE Trans. Antennas Propagat.*, vol. 52, no. 11, pp. 2877–2884, Nov. 2004.

[10] L. Huang, W. L. Schroeder, and P. Russer, "Theoretical and experimental investigation of adaptive antenna impedance matching for multiband mobile phone applications," in *IEE Conference on Wideband and Multiband Antennas and Arrays.* Birmingham, UK: IEE, Sep. 2005.

[11] H. Suzuki, I. Ohba, T. Minemura, and T. Amano, "Frequency tunable antennas for mobile phone for terrestrial digital TV broadcasting reception," in *IEEE AP-S Int. Symp. and URSI National Radio Sci. Meeting*. Albuquerque, New Mexico: IEEE, Jul. 2006.

[12] H. A. Wheeler, "Fundamental limitations of small antennas," *Proceedings of the I.R.E.*, vol. 35, pp. 1479–1484, Dec. 1947.

[13] R. F. Harrington, "Effect of antenna size on gain, bandwidth and efficiency," *J. of Research of the Nat. Bureau of Standards*, vol. 64D, no. 1, pp. 1–12, Jan. 1960.

[14] R.E.Collin and S.Rothschild, "Evaluation of antenna q," *IEEE Trans. Antennas Propagat.*, vol. 12, no. 1, pp. 23–27, Jan. 1964.

[15] R.L.Fante, "Quality factor of general ideal antennas," *IEEE Trans. Antennas Propagat.*, vol. 17, no. 2, pp. 151–155, Mar. 1969.

[16] H. F. Pues and A. R. V. de Capelle, "An impedance-matching technique for increasing the bandwidth of microstrip antennas," *IEEE Trans. Antennas Propagat.*, vol. 37, no. 11, pp. 1345–1354, Nov. 1989.

[17] *Mobile and Portable DVB-T Radio Access Interface Specification*, EICTA Std., Rev. 1.0, Jan. 2004.

[18] W. L. Schroeder, A. A. Vila, and C. Thome, "Extremely small, wideband mobile phone antennas by inductive chassis mode coupling," in *36th European Microwave Conf. Proc.*, Manchester, UK, Sep. 2006.

[19] J. Holopainen, J. Vilanen, M. Kyro, C. Icheln, and P. Vainikainen, "Antenna for handheld DVB terminal," in *2006 IEEE Internatinal Workshop on Antenna Technology Small Antennas and Novel Metamaterials*, Mar. 2006.

[20] J. Villanen, J. Ollikainen, O. Kivekäs, and P. Vainikainen, "Coupling element based mobile terminal antenna structures," *IEEE Trans. Antennas Propagat.*, vol. 54, no. 7, pp. 2142–2153, Jul. 2006.

[21] P. Vainikainen, J. Ollikainen, O. Kivekäs, and I. Kelander, "Resonator-based analysis of the combination of mobile handset antenna and chassis," *IEEE Trans. Antennas Propagat.*, vol. 50, no. 10, pp. 1433–1444, Oct. 2002.

[22] ——, "Performance analysis of small antennas mounted on mobile handsets," in *COST 259 Final Workshop - The Mobile Terminal and Human Body Interaction*, Bergen, Norway, Apr. 2000.

[23] C. T. Famdie, W. L. Schroeder, and K. Solbach, "Numerical analysis of characteristic modes on the chassis of mobile phones," in *European Conference on Antenna and Propagation*, Nice, France, Nov. 2006.

[24] W. L. Schroeder, C. Tamgue Famdie, and K. Solbach, "Utilisation and tuning of the chassis modes of a handheld terminal for the design of multiband radiation characteristics," in *IEE Conference on Wideband and Multi-band Antennas and Arrays*, Birmingham, UK, Sep. 2005.

[25] C. T. Famdie, W. L. Schroeder, and K. Solbach, "Optimal antenna location on mobile phones chassis based on the numerical analysis of characteristic modes," in *37th European Microwave Conf. Proc.*, Munich, Germany, Oct. 2007.

[26] W. L. Schroeder, P. Schmitz, and C. Thome, "Miniaturization of mobile phone antennas by utilization of chassis mode resonances," in *German Microwave Conference – GeMiC*, Karlsruhe, 2006.

[27] R. M. Fano, "Theoretical limitations on the broadband matching of arbitrary impedances," *J. Franklin Inst.*, vol. 249, pp. 57–83, Jan. 1950.

[28] A. R. Lopez, "More on narrowband impedance-matching limitations," *IEEE Antennas Propagat. Mag.*, vol. 46, no. 6, pp. 102–90, Dec. 2004.

[29] W.-K. Chen, *Theory and Design of Broadband Matching Networks.* Oxford: Pergamon Press, 1976.

[30] W. E. McKinzie III, "A modified Wheeler cap method for measuring antenna efficiency," in *Proc. IEEE Antennas and Propagation Society Int. Symp. Digest.* Montreal: IEEE, Jul. 1997, pp. 542–545.

[31] *Technical Specification Group Radio Access Network; User Equipment (UE) radio transmission and reception (FDD)*, 3rd Generation Partnership Project TS 25.101, Rev. V5.15.0, Jun. 2005.

[32] S. M. Sze and K. K. Ng, *Physics of Semiconductor Devices, third edition.* New York: John Wiley & Sons Inc., 2006.

[33] J. H. Schaffner, R. Y. Loo, D. F. Sievenpiper, F. A. Dolezal, G. L. Tangonan, J. S. Colburn, J. J. Lynch, J. J. Lee, S. W. Livingston, R. J. Broas, and M. Wu, "Reconfigurable aperture antennas using RF MEMS switches for multi-octave tunability and beam steering," in *Proc. IEEE Antennas and Propagation Society Int. Symp. Digest.* Salt Lake City: IEEE, 2000.

[34] I. Bahl and P. Bhartia, *Microwave Solid State Circuit Design*, 2nd ed. New York: Wiley & Sons Inc., 2003.

[35] K. Chang, *Handbook of RF/Microwave Components and Engineering*, 2nd ed. New York: Wiley & Sons Inc., 2003.

[36] V. Sokolov, J. J. Geddes, A. Contolatis, P. E. Bauhahn, and C. Chao, "A Ku-band GaAs Monolithic Phase Shifter," *IEEE Trans. Microwave Theory Tech.*, vol. 31, pp. 1077–1082, 1983.

[37] N. K. Osbrink, "YIG-tuned oscillator fundamentals," *Microwave Sys. News*, vol. 13, pp. 207–225, 1983.

[38] C. Liu, *Foundations of MEMS*, 1st ed. New York: Prentice Hall, 2005.

[39] Q. Han, K. Inagaki, and T. Ohira, "Perturbation analysis and experimental verification of intermodulation and harmonic distortion for an anti-series varactor pair," *IEICE Trans.*, vol. 88-C, no. 1, pp. 89–97, Jan. 2005.

[40] C. Balanis, *Antenna Theory Analysis and Design, second edition.* New York: John Wiley & Sons Inc., 1997.

[41] D. Agahi and W. Domino, "Efficiency measurements of portable-handset antennas using the Wheeler cap," *Applied Microwave and Wireless*, vol. 12, no. 6, pp. 34–42, Jun. 2000.

[42] R. Chair, K. M. Luk, and K. F. Lee, "Radiation efficiency analysis on small antenna by Wheeler cap method," *Microwave and Optical Technology Letters*, vol. 33, no. 2, pp. 112–113, Apr. 2002.

[43] *Technical Specification Group GSM/EDGE Radio Access Network; Radio transmission and reception*, 3rd Generation Partnership Project TS 45.005, Rev. V6.10.0, Jun. 2005.

[44] P. B. Johns and R. L. Beurle, "Numerical solution of 2-dimensional scattering problems using a transmission-line matrix," *IEE Proc.*, vol. 118, pp. 1203–1208, Sep. 1971.

[45] W. J. R. Hoefer, "The transmission line matrix method-theory and application," *IEEE Trans. Microwave Theory Tech.*, vol. 33, pp. 882–893, Oct. 1985.

[46] ——, "The transmission line matrix (TLM) method," in *Numerical Techniques for Microwave and Millimeter Wave Passive Structures* (T. Itoh, ed.), pp. 496–591, 1989.

[47] C. Christopoulos, *The Transmission-Line Modeling Method TLM.* New York: IEEE Press, 1995.

[48] P. Russer, "The transmission line matrix method," in *Applied Computational Electromagnetics,* NATO ASI Series, pp. 243–269, 2000.

[49] C. Christopoulos and P. Russer, "Application of TLM to microwave circuits," in *Applied Computational Electromagnetics,* NATO ASI Series, pp. 300–323, 2000.

[50] ——, "Application of TLM to EMC problems," in *Applied Computational Electromagnetics,* NATO ASI Series, pp. 324–350, 2000.

[51] P. Russer, *Electromagnetics, Microwave Circuit and Antenna Design for Communications Engineering, second edition.* Boston London: Artech House, 2006.